# Multi-Modal and Multi-Temporal Data Fusion: Outcome of the 2012 GRSS Data Fusion Contest

Christian Berger, Michael Voltersen, Robert Eckardt, Jonas Eberle, Thomas Heyer, Nesrin Salepci, Sören Hese, Christiane Schmullius, Junyi Tao, *Student Member, IEEE*, Stefan Auer, Richard Bamler, *Fellow, IEEE*, Ken Ewald, Michael Gartley, John Jacobson, Alan Buswell, Qian Du, *Senior Member, IEEE*, and Fabio Pacifici, *Member, IEEE*

***Abstract*—The 2012 Data Fusion Contest organized by the Data Fusion Technical Committee (DFTC) of the IEEE Geoscience and Remote Sensing Society (GRSS) aimed at investigating the potential use of very high spatial resolution (VHR) multi-modal/multi-temporal image fusion. Three different types of data sets, including spaceborne multi-spectral, spaceborne synthetic aperture radar (SAR), and airborne light detection and ranging (LiDAR) data collected over the downtown San Francisco area were distributed during the Contest. This paper highlights the three awarded research contributions which investigate (*i*) a new metric to assess urban density (UD) from multi-spectral and LiDAR data, (*ii*) simulation-based techniques to jointly use SAR and LiDAR data for image interpretation and change detection, and (*iii*) radiosity methods to improve surface reflectance retrievals of optical data in complex illumination environments. In particular, they demonstrate the usefulness of LiDAR data when fused with optical or SAR data. We believe these interesting investigations will stimulate further research in the related areas.**

***Index Terms*—Data fusion, LiDAR, multi-modal, multi-temporal, optical, SAR, urban, VHR imagery.**

Manuscript received November 06, 2012; revised January 16, 2013; accepted January 21, 2013. Date of publication March 15, 2013; date of current version June 17, 2013. This work was supported in part by the IEEE Geoscience and Remote Sensing Society (GRSS), DigitalGlobe, Inc., and the National Air and Space Intelligence Center (NASIC) under the Advanced Technical Exploitation Program (ATEP) Contract FA8604-09-D-7976.

C. Berger, M. Voltersen, R. Eckardt, J. Eberle, T. Heyer, N. Salepci, S. Hese, and C. Schmullius are with the Department for Earth Observation, Institute of Geography, Friedrich-Schiller-University Jena, Loebdergraben 32, D-07743 Jena, Germany (corresponding author e-mail: christian.berger@uni-jena.de).

J. Tao is with the Remote Sensing Technology Institute (IMF), German Aerospace Center (DLR), 82234 Oberpfaffenhofen-Wessling, Germany.

S. Auer is with the Chair of Remote Sensing Technology, Technische Universität München, 80333 München, Germany.

R. Bamler is with the Remote Sensing Technology Institute (IMF), German Aerospace Center (DLR), 82234 Oberpfaffenhofen-Wessling, Germany, and also with the Chair of Remote Sensing Technology, Technische Universität München, 80333 München, Germany.

K. Ewald and A. Buswell are with Ball Aerospace and Technologies, Fairborn, OH 45324 USA.

M. Gartley is with the Center for Imaging Science, Rochester Institute of Technology, Rochester, NY 14623 USA.

J. Jacobson is with theNational Air & Space Intelligence Center, Wright Patterson AFB, OH 45433 USA.

Q. Du is with the Department of Electrical and Computer Engineering, Mississippi State University, Mississippi State, MS 39762 USA.

F. Pacifici is with DigitalGlobe Inc., Longmont, CO 80503 USA.

Color versions of one or more of the figures in this paper are available online at http://ieeexplore.ieee.org.

Digital Object Identifier 10.1109/JSTARS.2013.2245860

## I. Introduction

THE Data Fusion Contest has been annually organized by the Data Fusion Technical Committee [1] of the IEEE Geoscience and Remote Sensing Society (GRSS) since 2006 [2]–[6]. It is open not only to IEEE members, but to everyone, with the aim of developing new or evaluating existing methodologies at the research or operational level to solve remote sensing problems using data from different sources. It has earned international reputation for providing high-quality data and promoting the cutting-edge research of remote sensing image processing and analysis.

The 2012 Contest was designed to investigate the potential use of very high spatial resolution (VHR) multi-modal/multi-temporal image fusion for various remote sensing applications. Three different types of data sets, including spaceborne multi-spectral (i.e., QuickBird and WorldView-2) and synthetic aperture radar (SAR) data (i.e., TerraSAR-X), and airborne (LiDAR) data, were provided by DigitalGlobe, Astrium Services, and the United States Geological Survey (USGS).

Fusion of multi-source images and data is considered to be the ultimate solution for optimized information exploitation in remote sensing [7]. Passive optical sensors have been widely employed to map horizontal structures like land cover (LC) types at broad scales. SAR complements optical imaging capabilities because of the minimum constraints on time-of-day and atmospheric conditions, and because of the unique responses of terrain and man-made targets to radar frequencies. Airborne LiDAR can provide highly accurate sample measurements (single pulse, multiple pulses, or even full waveform) of vertical structures, but it is currently limited by the high cost of acquisition. Thus, fusion of optical/SAR/LiDAR data can offer additional information for various applications, such as LC mapping [5], forest-related studies [8]–[12], oil slick detection and characterization [13], and accurate digital surface model (DSM) and digital elevation model (DEM) generation [7]. More recently, due to its increased availability, hyperspectral imagery and its fusion with LiDAR data have been of great interest for practical applications [14]–[20].

The data sets distributed during the Contest were acquired over the downtown San Francisco area, covering a number of large buildings, skyscrapers, commercial and industrial structures, a mixture of community parks and private housing, as well as highways and bridges. The composition of the optical, SAR, and LiDAR data sets is shown for a small subset in Fig. 1. As listed in Table I, the QuickBird/WorldView-2/TerraSAR-X data sets were acquired in late 2007 and 2011, while the LiDAR

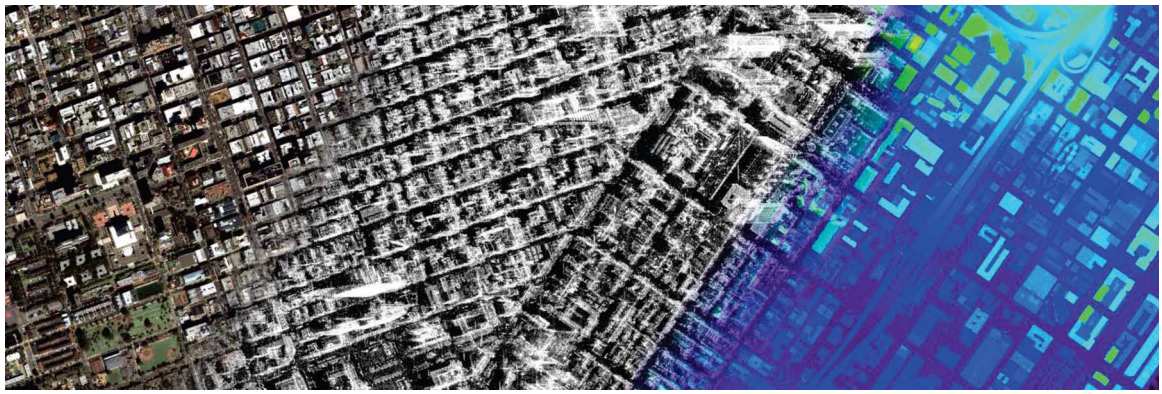

Fig. 1. Composition of the optical, SAR, and LiDAR data sets over the downtown San Francisco area.

TABLE I
SENSORS AND ACQUISITION DATES FOR THE IMAGES DISTRIBUTED DURING THE CONTEST

| Sensor | Acquisition 1 | Acquisition 2 |
|---|---|---|
| QuickBird/WorldView-2 | 11 November 2007 | 9 October 2011 |
| TerraSAR-X | 5 December 2007 | 2 October 2011 |
| | 16 December 2007 | 13 October 2011 |
| | 27 December 2007 | 24 October 2011 |
| LiDAR | June 2010 | |

data were collected in June 2010. Three products were derived from the raw LiDAR data in advance, including a DEM, a DSM and an intensity image. For this purpose, the LP360 software for ArcGIS was used. The DEM was created by triangulating elevation only from the bare-earth LiDAR points, while the DSM was created by triangulating elevation only from the first-return LiDAR points. And finally, the intensity layer was generated by triangulating intensity from the first-return LiDAR points.

More than 1150 researchers across the globe registered to the Contest, corresponding to an increase of more than 51% over the previous year. The data sets were downloaded by practitioners from 78 different countries, with a large number from developing and underdeveloped countries. This clearly demonstrates that the Data Fusion Contest is of great interest to the Earth observation research and application community.

To enter the Contest, each participant was asked to submit a paper describing the problem addressed, the method used, and the final results. Several interesting contributions were received, the large majority of which investigated the fusion problem for urban LC classification and change detection, followed by image pansharpening. Other topics included automated road extraction, moving object detection, urban tree inventory, and image superresolution, demonstrating the large variety of applications that multi-modal/multi-temporal remote sensing images can offer.

After rigorous review by the Data Fusion Award Committee, three winning papers were selected, and their authors were awarded IEEE GRSS Certificates of Appreciation during the 2012 IEEE International Geoscience and Remote Sensing Symposium (IGARSS) held in Munich, Germany.

In the remainder of this paper, the contributions proposed by the three winning teams are described in detail. Specifically, Section II presents the work of C. Berger, M. Voltersen, R. Eckardt, J. Eberle, T. Heyer, N. Salepci, S. Hese, and C. Schmullius, from the Friedrich-Schiller-University of Jena, Germany, who fused WorldView-2 and LiDAR data to derive a new metric for the assessment of urban density (UD) by taking into account both horizontal and vertical characteristics of a city. In Section III, a simulation-based method to jointly use TerraSAR-X and LiDAR data for image interpretation and change detection in dense urban areas is proposed by J. Tao, S. Auer, and R. Bamler from the German Aerospace Center and Technische Universität München, Germany. Section IV illustrates the research of K. Ewald and A. Buswell from Ball Aerospace and Technologies Corp., M. Gartley from the Rochester Institute of Technology, and J. Jacobson from the National Air and Space Intelligence Center, United States, on a technique using radiosity methods to improve surface reflectance retrievals from WorldView-2 data in complex illumination environments. Finally, the conclusions and perspectives drawn from this Contest are presented and discussed in Section V.

## II. FUSION OF MULTI-SPECTRAL AND LIDAR DATA FOR AN INTEGRATED ASSESSMENT OF URBAN DENSITY (UD)

This section aims at the derivation of a new indicator to assess UD (defined here as the intensity of urban development) that takes into account all three spatial dimensions of a city. In fact, the presence of building objects adds a third dimension to be considered among the environmental relationships found in urban areas. Thus, urban environmental studies should rely on information sources that account not only for the horizontal dimensions, but also for the vertical dimension of a city to enable a more holistic assessment of the *builtscape* [21].

To assess UD, a variety of spatial indicators has been used in the past. In general, these indicators can be subdivided into two groups: (*i*) two-dimensional (2D), and (*ii*) three-dimensional (3D) indicators. While 2D indicators measure the percentage of specific urban LC classes within a predefined area of interest (AOI), 3D indicators quantify information related to the height or volume of objects belonging to specific urban LC classes within the AOI. To calculate the 2D indicators, *a priori* information about urban LC is required. In addition to urban LC, 3D indicators do also require information about the height of urban LC objects. The AOI used to infer those indicators can

be a single pixel, a grid cell, or a moving window (kernel) summarizing groups of classified pixels [22], [23], but can also be a circle of a certain radius around specific urban LC objects [24] or an administrative area like a zoning district, tax parcel or a land lot [25], [26]. If the AOI is a single pixel (2D indicators only), the indicator is computed by analyzing the proportion of specific urban LC classes at the sub-pixel level using spectral unmixing techniques [27]–[31].

A common 2D indicator of UD is the impervious surface area (ISA), also known under various other names [22], [23], [27], [28], [32]. Often provided as percentage [27]–[30], [33], the ISA is defined as the share of impervious surfaces within an AOI. A similar 2D indicator is the building coverage ratio (BCR) [25], [26], [34], [35]. As bare soil areas usually do not cover more than 5% of a city, the abundance of impervious surfaces is found to be inversely related to the abundance of urban vegetation [31], [36]. For this reason, it is also possible to describe UD by the intensity of urban greenery. In this regard, a widely used 2D indicator is the vegetation fraction (VF) [37]–[40]. VF evaluates the percentage of urban green within an AOI. Schöpfer *et al.* [41] extended the VF by introducing additional criteria and weighting factors to its calculation. As a result, VF values depend not only on the amount of urban vegetation, but also on the percentage of high-rise buildings and the distance between buildings found within the AOI.

Only few 3D indicators of UD can be found in the scientific literature. Among them, the floor area ratio (FAR) has been discussed in [25], [26], [35]. It represents the ratio of the gross floor area of one or more buildings within an AOI and the total area of the AOI. For its estimation, a constant value representing the average height of one story of all buildings under consideration has to be specified. Another 3D indicator is the vegetation volume to built-up volume (VV2BV) [24], which describes the relation between the cubic volume of high vegetation and the cubature of buildings within an AOI. The VV2BV was developed to better characterize the living quality in cities. A further 3D indicator related to vegetation is the green plot ratio (GPR) [42]. It is defined as the average leaf area index (LAI) of urban greenery within the AOI. For example, a site with a GPR of 2:1 features vegetation that has a total canopy cover twice that of the site. Because the LAI measures the area of leaves per area of ground, the concept behind the GPR takes into account the area that is covered by multiple, vertically-arranged canopy layers within the AOI.

The above selection of studies shows that various spatial indicators of UD have been proposed and used so far. However, it has to be kept in mind that each of these indicators considers different and distinct characteristics of human settlements and, thus, addresses only specific aspects of UD. Consequently, there is a lack of comprehensive indicators that are able to interrelate existing and possibly new spatial indicators for a more holistic assessment of density patterns in urban environments. An exception to this observation are the Spacematrix and the urban vegetation index (UVI). The Spacematrix is a 3D feature space to describe UD within an AOI [34]. This feature space is spanned by the indicators road network density (N), FAR, and BCR [34], and was successfully used to investigate the relation between traffic noise and UD [35]. The UVI represents the weighted sum of two ratios, namely the VV2BV and the vegetation area to built-up area ratio, and was recently employed for an improved assessment of both urban green spaces and urban quality of life [24]. Apart from these exceptions, there is still a need for integrated approaches making use of a combination of 2D and 3D indicators to estimate UD in its entirety. In the following subsections, this need is addressed by a combined indicator that takes into account four different key features of the urban landscape.

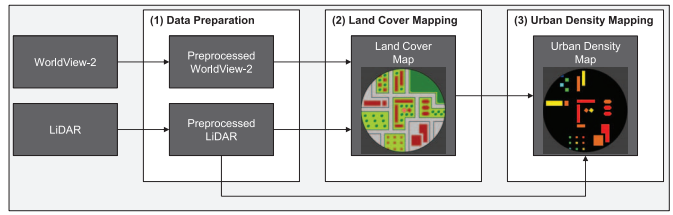


Fig. 2. Conceptual workflow for the assessment of urban density.

### A. Proposed Method

The overall workflow of this study consists of three consecutive steps: (*i*) data preparation, (*ii*) LC mapping, and (*iii*) UD mapping. Fig. 2 illustrates the role of the data sets being used in the context of each stage of the data fusion approach. After data preparation, LC is extracted from the preprocessed WorldView-2 and LiDAR data by means of feature fusion [43]. The LC map is then utilized in combination with the object height information provided by the LiDAR data to infer UD.

*1) Data Preparation:* Preprocessing of the WorldView-2 imagery comprises three separate steps: (*i*) radiometric normalization using ATCOR [44], (*ii*) pansharpening using the high-pass filter (HPF) fusion [45], and (*iii*) co-registration to the LiDAR data using more than 20 well-distributed ground control points (GCPs) and the DEM. A normalized digital surface model (nDSM) is calculated from the LiDAR data by subtracting the DEM from the DSM. It contains the height of urban objects relative to the ground. With respect to the LC classification, additional features are derived from the input data. Amongst those features are the average reflectance of the blue, green, red, and the first near-infrared (NIR) WorldView-2 bands, the normalized difference vegetation index (NDVI) [46] and the slope (in percent) of the nDSM [47]. The latter is useful for identifying transitions between flat areas and elevated objects (e.g., trees or buildings) [48].

*2) Extraction of Land Cover (LC) Information:* Six LC classes are extracted from the data basis: buildings, impervious surfaces, trees, grass/shrubs, bare soil areas and water bodies. For this purpose, an object-based image analysis (OBIA) approach [49]–[51] is employed for its advantages over traditional, pixel-based classification techniques with respect to feature extraction from VHR multi-source imagery [49], [52]–[56]. A complete description and evaluation of the method (implemented in Trimble eCognition), including a discussion on its robustness with regard to four different multi-spectral and LiDAR input data sets acquired over three urban areas, is provided in Berger *et al.* [57].

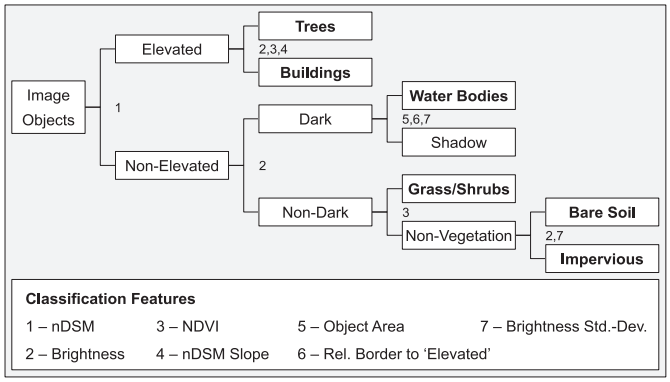


Fig. 3. The land cover mapping scheme applied to the image objects.

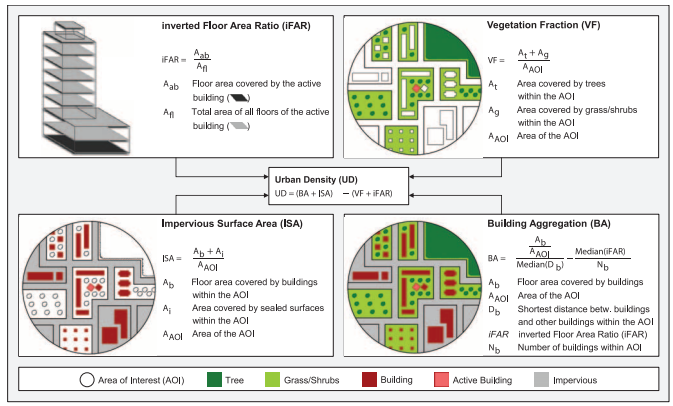


Fig. 4. The four input parameters used to infer urban density.

As a first step, a number of segmentation algorithms is applied to the input data. Subsequently, a rule-based classification of the resulting objects is performed following the scheme in Fig. 3. The numbers at each node of the decision tree indicate the features that are used for class separation. As an example, the tree canopy class is considered. Image segments are first divided into elevated and non-elevated objects using the LiDAR nDSM. To this end, an adjustable object height value serves as threshold for classification. Afterwards, elevated objects are reclassified as tree canopy if they feature a relatively high NDVI. Finally, the resulting tree canopy objects are used as seeds which are grown into adjacent pixels belonging to the elevated class if the latter have similar, but not necessarily as distinct, NDVI and brightness characteristics as the former. In a way similar to the tree canopy class, these so-called pixel-based object resizing operations [58] are also used to grow and/or shrink objects of other LC types. After the extraction of the six target classes, some reshaping algorithms are applied to the thematic objects for the purpose of border optimization. For instance, building footprints are generalized by calculating a morphological parameter called surface tension [58] and evaluating the result against a predefined criterion of compactness. In this way, the original object primitives are successively transformed into more meaningful objects of interest that better correspond to the visual perception of humans [49], [59]–[61]. Finally, all remaining shadow objects are reassigned to the class with which they share the largest relative common border.

To assess mapping accuracy, two data sources are used. The building class is validated using the building footprints provided by the City of San Francisco [62], whereas the remaining LC types are validated using the panchromatic WorldView-2 band. A random sampling design is chosen for validation comprising 50 sample points per LC class to assess overall accuracy, errors of commission and omission, as well as the kappa coefficient of agreement [63], [64].

*3) Derivation of Urban Density (UD) Information:* UD values are calculated for each single building (referred to as *active* building) in the LC map and within a predefined radius (i.e., the AOI) around the centroid of the respective building. They are the result of a logical combination of four parameters quantifying (*i*) vertical development, (*ii*) urban vegetation, (*iii*) soil sealing, and (*iv*) the clustering of urban structures within the AOI (Fig. 4). Since each of these input variables evaluates a different and distinct aspect of the *builtscape* [21], the resulting information layer enables an integrated and more holistic assessment of local UD patterns.

The parameters used to assess UD are the inverted floor area ratio (iFAR), VF, ISA and building aggregation (BA):

- *iFAR* describes the ratio between the footprint and the gross floor area of an active building [25], [26], [35]. It ranges between 0 and 1. UD decreases with higher values of iFAR.
- *VF* describes the urban green area ratio within the AOI [37]–[40]. It ranges between 0 and 1. UD decreases with higher values of VF.
- *ISA* describes the degree of soil sealing within the AOI [27]–[30], [33]. It ranges between 0 and 1. UD increases with higher values of ISA.
- *BA* describes the arrangement and compactness of buildings within the AOI. For the calculation of BA, the median building distances as well as the median iFAR values of all buildings within the AOI are used. BA is normalized between 0 and 1 to match its values to the range of other input parameters. UD increases with higher values of BA.

Finally, UD represents an example for describing the intensity of urban development in its entirety, i.e., with regard to horizontal and vertical settlement characteristics. It is obtained by linking/integrating the above selected indicators as depicted in Fig. 4. The index is designed in a way that the individual and unique contributions coming from its inputs are mutually reinforced. That is why UD is formulated as the difference between two terms. The left term of the expression is proportional to UD and increases if BA and/or ISA increase, whereas the right term of the expression is inversely proportional to UD and increases if VF and/or iFAR increase. Given the dynamic range of its input parameters, UD ranges between −2 and +2 (from low to high intensity of urban development).

## B. Results and Discussion

The resulting LC map is shown in Fig. 5. An overall area of about 30 km$^2$ has been classified. Since the study area is close to downtown San Francisco, the largest areal coverage is observed for sealed surfaces (43.2%) and buildings (20.6%). Together with the small coverage of the vegetation classes (7.9%), this is a first indicator of the high overall degree of UD found in the area. The user's and producer's accuracies of

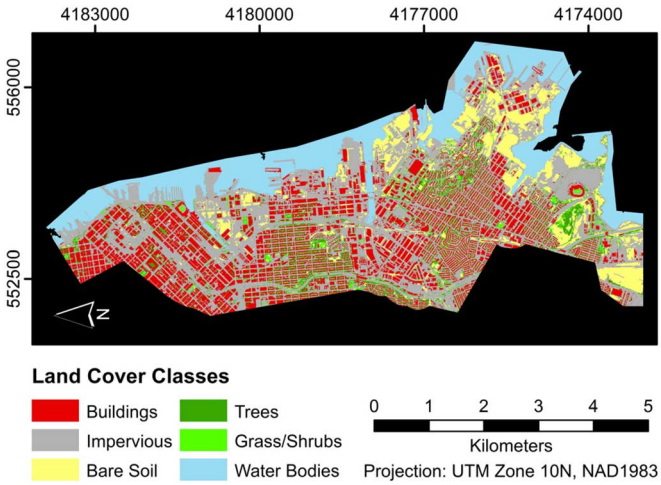


Fig. 5. Land cover map of the study area in San Francisco.

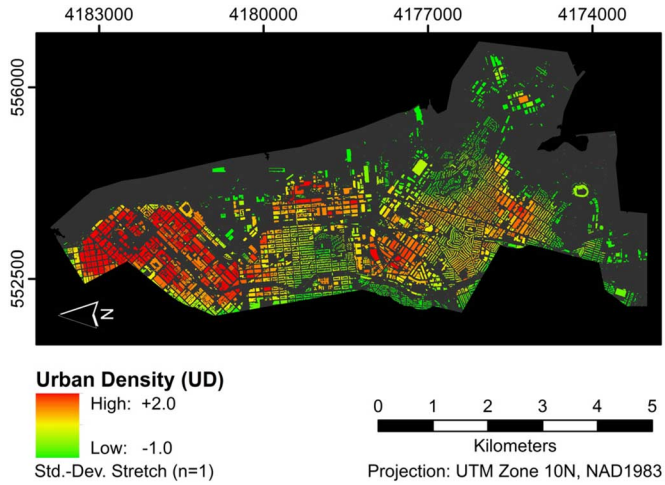


Fig. 6. Urban density map of the study area in San Francisco.

the LC map are consistently above 80.0%, and in many cases even above 90.0%. Smaller errors of commission and omission mainly occur because of the rather simple classification rules applied to the image objects (see Fig. 3). Examples are the misclassification of very high bridges as buildings (instead of impervious) or the confusion between bare soil areas and sealed surfaces [27], [28], [65]–[69]. Apart from these classification errors, the overall accuracy of the LC map is 88.0% and the kappa coefficient amounts to 0.86.

The UD map derived for the study area is shown in Fig. 6. More than 5,000 buildings have been attributed with UD values. While high UD values are indicated by red color, medium, moderate and low UD values are expressed by orange, yellow and green tones, respectively. The AOI used for the calculation of UD corresponds to a radius of 250 m around the centroid of each building object. To compute the area of individual floors of a single building (i.e., to calculate iFAR), a mean floor height of 2.8 m is assumed [25]. The largest patch featuring high to medium UD values (up to +1.9) is located in the north of the scene. Three smaller UD hot spots are distributed across the rest of the area. Moderate to low UD values (as low as $-1.0$) are found in the western, southern and south-eastern regions of the map. In the north, the high degree of horizontal and vertical development (ISA and iFAR) paired with the large number of buildings (BA) and the small urban green area ratio (VF) lead to the largest UD values for the entire scene, whereas these conditions are inverted for the western, southern and south-eastern regions of the map leading to the smallest UD values.

To further investigate the validity of the UD map, UD box plots for and locations of six selected land use (LU) types [70] are presented in Fig. 7. Since the radius of the AOI used is 250 m, LU polygons that are closer than 250 m to the edge of the study area are excluded from the analysis to obtain error-free UD statistics. A comparison of the median values (red dashes) for each LU class suggests that UD is able to consistently reproduce the increasing degree of urban development that can be expected in dependence of the LU type considered. While the median UD is low for the residential classes (RM, RH), UD steadily rises with actual settlement density in industrial areas (PDR) until it reaches its peak for the downtown classes in the north of the scene (DR, SM, DC). Besides these trends of urban densification, Fig. 7 also shows that UD values are generally high (between 0.2 and 1.9) for all LU classes and no negative values occur at all. This is in good agreement with the fact that the study area covers a central part of San Francisco. In conclusion, these findings underline the validity and suitability of the proposed UD metric as a useful measure to assess density patterns in urban environments. To increase the transparency of this contribution to the Data Fusion Contest, a dedicated geoportal was set up that visualizes all input data, final results, by-products, as well as additional information layers [71].

## III. Combination of LiDAR and SAR Data With Simulation Techniques for Image Interpretation and Change Detection

The visual interpretation of SAR images is difficult due to distortion effects related to the SAR imaging concept, whereas the detection of changes may be hampered by missing pre-event SAR data, different SAR acquisition configurations (especially changes of the incidence angle), and revisit time related to subsequent SAR acquisitions.

For SAR image interpretation, raw data simulators [72] and imaging simulators [73]–[76] have been developed. Raw data simulators focus on radiometric correctness and consider dielectric properties and roughness parameters of building materials for the radiometric interpretation [77]. SAR imaging simulators concentrate primarily on geometric correctness when using detailed building CAD-models with simplified surface material information as input. A detailed overview of different concepts for SAR simulation is given in [78]. So far, none of the simulators reported in the literature enables to provide geocoded simulated image for direct comparison with real SAR data. First attempts in the application of simulation techniques for damage assessment using high resolution SAR data are presented in [79] and are based on building parameters extracted manually from optical images. So far, LiDAR data have not been included in SAR simulation applications in a practicable and productive way.

The use of multi-temporal medium-high spatial resolution SAR data has been discussed in [80], [81] for unsupervised change detection methods. For very high spatial resolution SAR

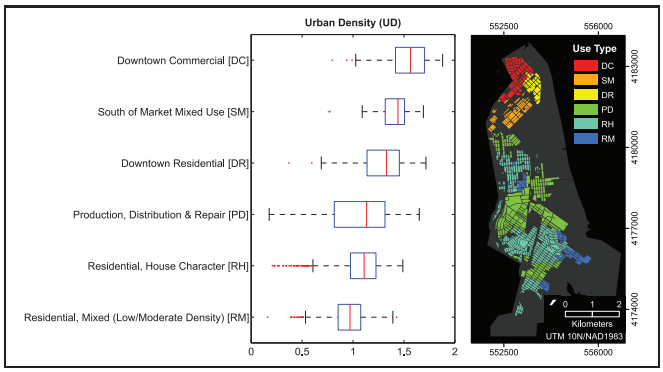


Fig. 7. Urban density box plots for the six selected land use types [70].

images, e.g., TerraSAR-X or COSMO-SkyMed, feature based change detection methods have been proposed in [82], [83]. One condition of all these multi-temporal analysis is that the images should be acquired with the same viewing configuration, in order to avoid high rate of false alarms in the final change detection result.

### *A. Proposed Method*

This section provides the details in three major steps: (*i*) interpret TerraSAR-X images of a dense urban area, (*ii*) detect changes between LiDAR data and TerraSAR-X data, and (*iii*) support an object-based multi-temporal SAR change analysis focusing on façade regularities:

*1) Automatic Interpretation of SAR Images Based on Simulation Techniques:* The TerraSAR-X product is first projected to a plane with constant height (frame mean height) on the WGS84 ellipsoid. The LiDAR image is converted to a DSM in the WGS-84 coordinate system with ellipsoidal heights. Finally, a DEM and an nDSM are generated from the DSM using the method described in [84]. Successfully, the SAR simulator RaySAR [85] is used to generate a simulated SAR image of the LiDAR DSM. Thereafter, the geoinformation of the DSM as well as the orbit and projection parameters of the real SAR image are used to geocode the simulated image. The generation and geocoding of the simulated SAR image using a DSM is detailed in [86]. Finally, the simulated signals of reflection levels 1 and 2 are combined into one image or are assigned to separate image layers [85] for the DSM, DEM, and nDSM, respectively. The simulated images are: image *A* (double reflections from DSM) and images *B*, *C*, and *D* (sum of all reflection levels for DSM, DEM and nDSM, respectively). Successively, the images are combined to generate five image layers:

- double reflection ($A > 0$)
- layover ($D > 0$)
- shadow ($B = 0$ & $C > 0$)
- background ($B = 0$ & $C = 0$)
- ground ($B > 0$ & $A = 0$ & $D = 0$)

The layer generation flow-chart is illustrated in Fig. 8.

*2) Change Detection Between LiDAR and SAR Data:* as the simulated images and the real SAR images are geocoded, they can be directly compared. As the focus of the simulation algorithm is on geometrical correctness, no comparison is carried out

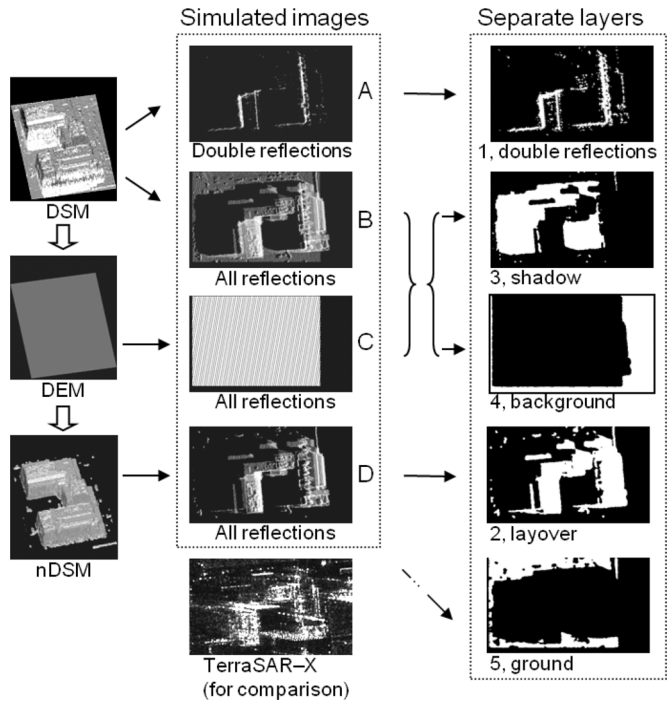


Fig. 8. Simulation of separate layers: from the elevation models (left), four simulated images are generated (center); the combination of them yields five image layers (right).

between simulated and real intensities. Instead, the geometric information provided by the simulated images is used, especially in the shadow and ground layers. If there is no change within the scene between the LiDAR and SAR acquisition dates, SAR image pixels in the shadow and ground layers should be mainly characterized by low intensity. Following this assumption, a pixel based algorithm is performed to detect positive changes of large extent in shadow and ground layers. To this end, an intensity threshold is determined by a statistical analysis of the SAR image for each layer. All pixels in the corresponding layer in the SAR image with intensities higher than the threshold value are considered as candidates of positive changes and will form regions in terms of changes of significant extent (see [87] for a detailed description).

*3) Object Based Change Detection Between Two SAR Images With Support of LiDAR Data Simulation:* In addition to the pixel based change detection between LiDAR and SAR data, simulation techniques that enable an object based change detection between two SAR images are also investigated.

For the extraction and simulation of single buildings and single walls, isolated parts in the nDSM exceeding a size threshold of 1500 pixels are selected as building of interest (see example in Fig. 9(a)). Similarly to the procedure described previously, three image layers can be generated for each building: layover, double bounce and shadow. As the analysis aims at individual façades, every building model is decomposed into separate wall segments. First, gradient magnitude (Fig. 9(b)) and gradient direction (Fig. 9(c)) maps are calculated and are convolved with a median filter. Second, a height threshold value is calculated in the neighborhood of the pixel with the highest gradient magnitude, using the mean

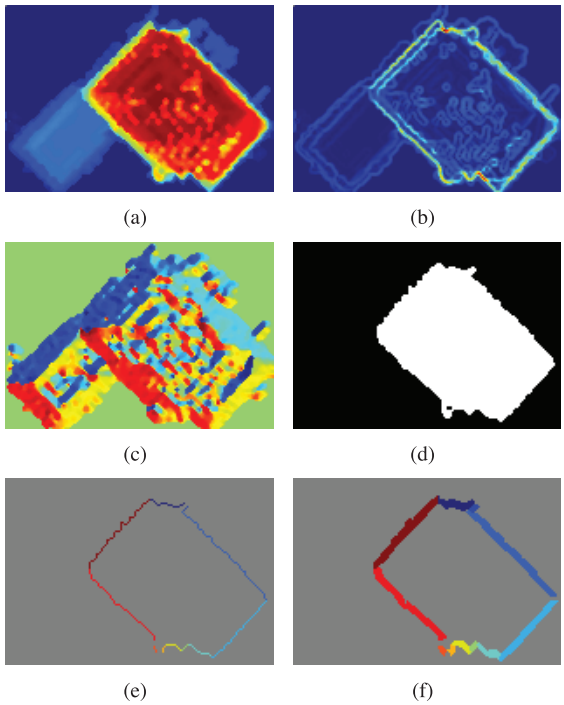


Fig. 9. Separation of building walls (DSM parts) for an individual building: (a) building extent in DSM, (b) gradient magnitude map, (c) gradient direction map, (d) building model after applying the height threshold, (e) separated building boundary segments, (f) extracted wall segments, different colors indicate different wall masks.

value of the maximal and minimal height. Third, after applying the height threshold (Fig. 9(d)), the building boundaries (with width of 1 pixel) are generated and separated according to the corresponding gradient direction values. Fourth, the separated boundary segments (Fig. 9(e)) are enlarged using the information of the neighborhood geometry and similar gradient direction, which yields separate wall masks (Fig. 9(f)). Finally, the simulation of the wall models provides the respective wall layover masks. A gradient direction difference is used as a threshold for separating the boundary in the third step. Low values lead to oversegmentation, for high values several building wall segments may be considered as one wall segment in the result. The suggested value is 30 degrees, which works for most of the rectangular buildings.

Regarding the façade characterization, SAR pixels located within the wall layover masks are extracted for identifying signature patterns. Dominant signatures in the layover area are likely to be related to façade structures, e.g., reflections at window corners [85]. Point signatures representing façades with regular structures tend to be distributed in range and wall direction, indicating the windows arrangement in vertical and horizontal direction, respectively. The analysis of the pattern topology may help convert pixel-based to object-based representations for identifying changes. Initial attempts in this direction are indicated as follows. First, the local maxima of the SAR amplitude image are extracted in the layover area (set of point signatures). Then, a weighted Hough transform, which emphasizes pixels identified as local maxima, is used to identify linear organized signatures (along the orientation direction of the façade and in range direction; see [88] for

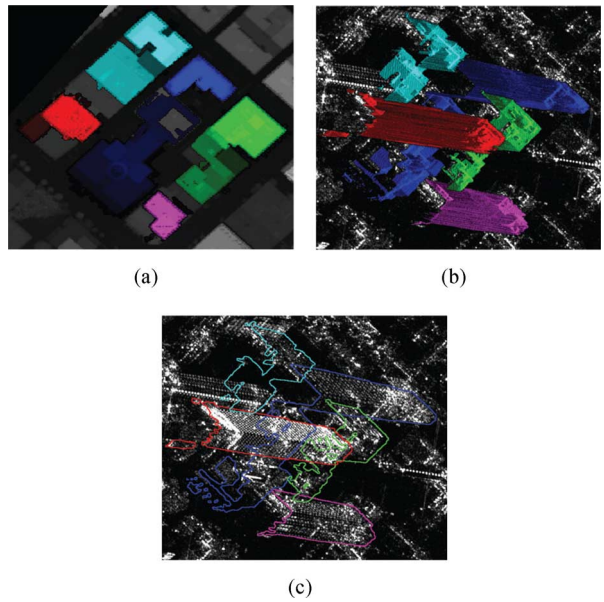


Fig. 10. Interpretation of SAR image in dense urban area: (a) individual building models; (b) simulated layover areas and (c) layover contours imposed on TerraSAR-X image. Different colors indicate different building models in the images.

further details). An object based representation of layover areas may be of great importance, because SAR images captured from different imaging geometries become comparable by analyzing differences of the pattern topology (for positive and negative changes).

### B. Results and Discussion

In order to assess the functionality of the proposed approach, the SAR simulation is combined with the LiDAR data and two TerraSAR-X images on a dense area with tall buildings in the northern part of the scene for SAR image interpretation and façade pattern recognition, and on the harbor area for change detection between LiDAR and SAR data.

In the first experiment, 203 building models with more than 1500 pixels are extracted from the DSM. As an example, five building models are shown in Fig. 10(a). The contours of the corresponding simulated layover, overlapped on the geocoded TerraSAR-X image, are depicted in Fig. 10(c). Different colors indicate different building models. The red model is the same building model as shown in Fig. 9. Parts of its layover area are overlapped with signal responses from the green and blue buildings. It is clearly seen which layover parts and, hence, signature patterns can be assigned exclusively to the red building. This helps understand why the façade of this red building in the real SAR image has an abnormal grammar in the overlapped area (see detailed view in Fig. 13).

For the harbor area, the simulated image, the geocoded TerraSAR-X image, the separate layers, and the detected positive changes in the shadow and ground layers are shown in Fig. 11. For a better representation, a rectangular area (visualized by a yellow frame) is extracted and shown in Fig. 12(a)–(d). Compared visually to the given LiDAR data (Fig. 12(e)) and the WorldView-2 image (Fig. 12(f)), the detected positive change can be confirmed. Due to the speckle effect of the SAR

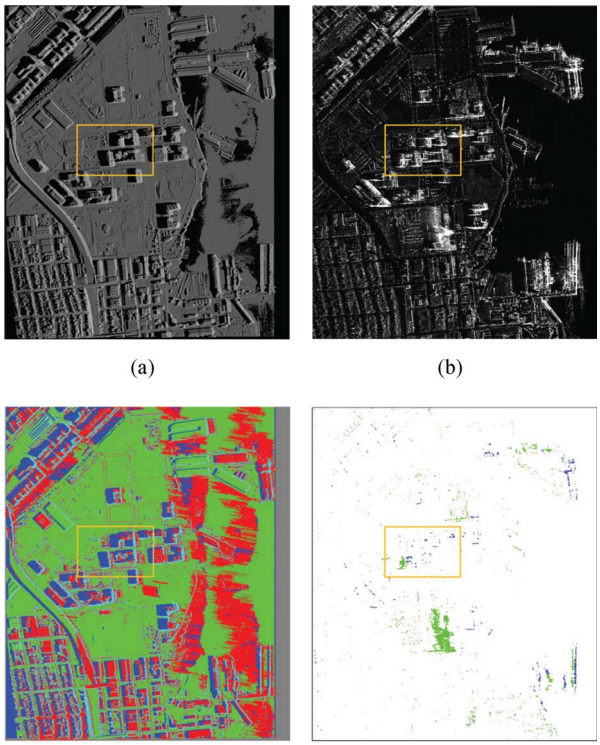


Fig. 11. Change detection between LiDAR and TerraSAR-X data: (a) geocoded simulated image from DSM, (b) geocoded TerraSAR-X image acquired on October 13, 2011, (c) separate layers (blue: shadow; green: ground; red: layover; cyan: double bounce; grey: background), (d) detected positive changes in shadow (blue) and ground (green) layer.

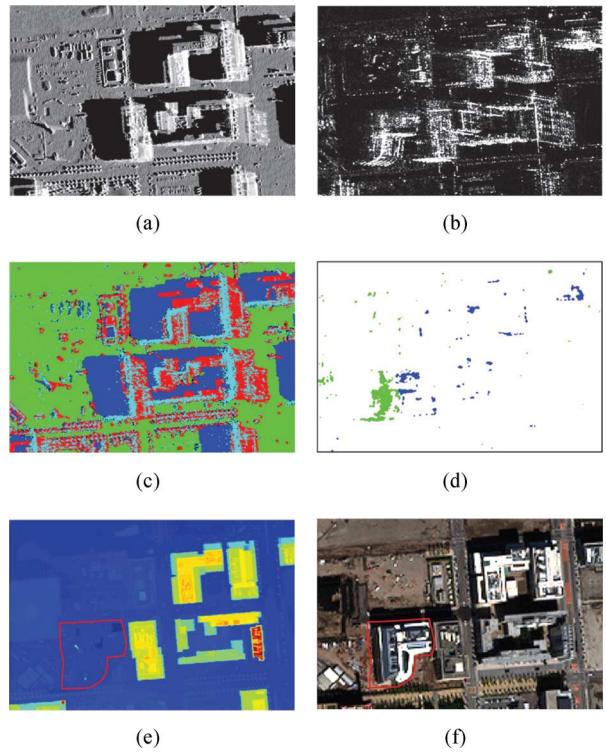


Fig. 12. Change detection between LiDAR and TerraSAR-X data (zoom in to rectangle marked area in Fig. 11), (a)–(d) images corresponding to those of Fig. 11, (e) LiDAR DSM with marked change, (f) WorldView-2 image showing a new building (marked in red).

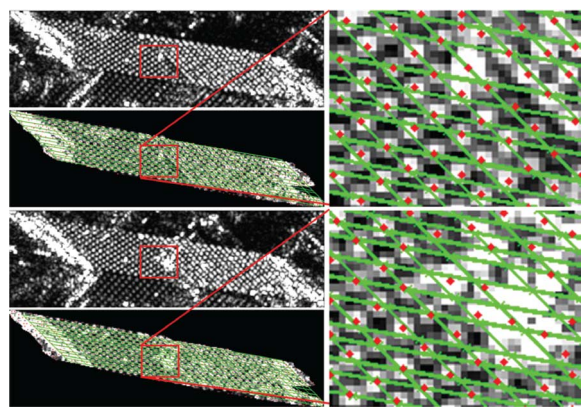

Fig. 13. Extracted signature pattern for the red building model in Fig. 10. Building layover in SAR image imposed with detected Hough lines. Red points: local intensity maxima. Acquisition dates: December 16, 2007 (upper two images), October 13, 2011 (lower two images).

sensor, which is not considered in the simulator, some small false alarms can be seen in the right upper corner.

As a change detection example, the red building model in Fig. 10 is chosen in order to analyze the appearance of point signatures. Among the 11 separated wall parts of the building model, two are chosen for façade pattern analysis according to their length and gradient direction (with respect to the SAR range direction). Fig. 13 shows the TerraSAR-X image and the imposed set of linearly organized signatures for the two image acquisition dates. Signature patterns extracted from layover areas provide the following information: the regularity of the pattern gives strong hints for the existence of buildings; distances between point signatures indicate distances between windows and floor heights; the number of floors and window columns can be counted in order to characterize the building topology. Although the signatures in the two TerraSAR-X images are not exactly the same, the topology of the pertinent patterns gives a strong hint that no significant changes are present.

## IV. Radiosity Technique for Reflectance Retrieval in Complex Illumination Environments

Remote sensing exploitation using spectral sensors in the visible through shortwave infrared relies on the ability to determine the reflectance of surface materials. Atmospheric compensation methods calculate the solar illumination, both direct from the sun and indirect from scattered sunlight. However, many targets of interest are in complex illumination environments where the surface is in shadows and, even in sunlit areas, nearby objects can block some of the downwelling sky radiance. In addition, the nearby objects such as building walls or trees may reflect radiation, providing their own source of illumination onto the target of interest. Current atmospheric compensation algorithms do not account for these illumination conditions that are more complex than a clear, hemispherical sky overhead for an object parallel to flat ground.

Many spectral processing techniques require an accurate retrieval of the surface reflectance from the measured radiance data. Some material detection techniques, in particular, compare

the retrieved reflectance to reflectance spectra from a spectral library [89]. To obtain a better estimate of surface reflectance, more accurate estimates of the illumination on the surface is needed. In addition, retrieval of material reflectance in shadow regions depends solely on the indirect illumination from downwelling scattered radiance and reflections from nearby surfaces.

This section presents a radiosity-based method to improve reflectance retrieval under complex illumination conditions by taking into account surface tilt, solar obscuration, and surface to surface interaction within the scene. The background and implementation of the radiosity method to solve for surface reflectivity is discussed in [90]. Improvements to reflectance retrieval are shown through application of the radiosity technique to multi-spectral WorldView-2 data.

### A. Proposed Method

Radiosity was first used to analyze heat transfer between surfaces [91]. While computationally intensive, the technique provided methods for computing radiant interchange between surfaces for many different applications. Computer graphics began to use radiosity as a way to calculate realistic looking scenes under specified lighting conditions. As computational capabilities have increased, radiosity has become a more capable method to create simulated scenes that are physically accurate.

The radiosity approach uses the energy balance of the surfaces in a scene to create a system of equations to solve for illumination [92]. Radiosity, which is equivalent to the radiant exitance, is related to the radiance of a surface by:

$$B(x) = \int_{\Omega} L(x, \theta, \phi) \cos\theta \, \partial\omega \tag{1}$$

where $L(x, \theta, \phi)$ is the outgoing radiance at a point defined by the location $x$ in the direction defined by $\theta$ and $\phi$. For ideal diffuse surfaces, the outgoing radiance is a function of the position and the radiosity can be simplified to:

$$B(x) = \pi L(x) \tag{2}$$

The general global illumination equation describes the energy equilibrium for a set of radiating surfaces where the radiance leaving point $x$ in direction $(\theta_0, \phi_0)$ is given by:

$$L(x, \theta, \phi) = L_e(x, \theta_0, \phi_0) + \int_{\Omega} \rho_{\mathrm{bd}}(x, \theta_0, \phi_0, \theta, \phi) + L_i(x, \theta, \phi) \cos\theta \, \partial\omega \tag{3}$$

where the first term, $L_e$, is the emitted radiance in the direction $(\theta_0, \phi_0)$ at point $x$, and the integral term is the reflected radiance due to light incident at $x$ from all other directions in the hemisphere $\Omega$ with the bidirectional reflectance distribution function of the surface at point $x, y$ given by $\rho_{\mathrm{bd}}$.

Using the definition of radiosity and discretizing the problem leads to the discrete radiosity equation [93]–[95] which is:

$$B_i = E_i + \rho_i \cdot \sum_{j=1}^{N} F_{ji} B_j \tag{4}$$

where $E_i$ is the emitted radiance for a small patch $i$ (set to zero for visible through shortwave infrared wavelengths), $\rho_i$ is the diffuse reflectance at patch $i$ (unknown to be solved for), $F_{ji}$ is the form factor giving the solid angle subtended by the patch $j$ onto patch $i$ (solved for using scene geometry), $B_j$ is the radiosity of patch $j$ (retrieved from sensor data), and $N$ is the total number of surfaces in the scene (obtained during scene and sky facetization).

The discrete radiosity equation solves for radiosity given a surface's known reflectivity and illumination. The problem in remote sensing is to solve the inverse problem: given a scene with known radiosity of each surface, solve for the surface illumination to estimate reflectivity. This procedure is known as the inverse global illumination [91]. Equation (4) can be rearranged to solve for reflectivity. Setting the emitted radiance to zero, we obtain the radiosity equation for reflective surfaces:

$$\rho_i = \frac{B_i}{\sum_{j=1}^{N} F_{ji} B_j} \tag{5}$$

This is equivalent to the ratio of the outgoing radiance to the incoming radiance $(\varphi_{\mathrm{out}}/\varphi_{\mathrm{in}})$. To use the radiosity equation to estimate surface reflectance, a 3-dimensional model of the scene needs to be developed to determine which surfaces see each other and to calculate the form factors, $F_{ji}$. This is achieved by dividing the geometry into discrete facets including both the objects in the scene as well as the hemispherical skydome. The discrete facets in the 3-dimensional model are generated using both the geometry of the scene and the measured radiance to obtain surface facets with near uniform radiance. In addition, the geometric model can be used to determine which sections of the sky illuminate each facet through the form factor calculation. The illumination on each surface can be calculated using the radiosity equation taking into account the radiance from other surface and sky facets that are visible from that surface.

In this research, the process to determine the surface reflectance using radiosity combines processing the geometry data from LiDAR and the spectral data. Fig. 14 shows the process flow.

The first step in the processing chain is to estimate the surface-leaving radiance by removing the atmospheric effects on the collected imagery. During this step, the data is converted from at-sensor radiance to surface-leaving radiance, which equate to the $B_i$ terms in the radiosity equation. For radiometrically calibrated spectral data, such as that from WorldView-2, atmospheric parameters are retrieved using the radiative transfer code MODTRAN [96]. During this step, path radiance is estimated and then subtracted from the sensor radiance. The remaining signal is radiance from the target itself that reaches the sensor. The sensor-to-ground transmission losses are accounted for by dividing the at sensor target radiance by a MODTRAN-derived transmission estimate to produce the signal that would be observed from placing the sensor at the ground, which equates to the surface leaving radiance.

During the atmospheric retrieval step, MODTRAN is also used to estimate downwelling radiance at various azimuth and elevation angles. This allows for an accurate representation of the directional spectral radiance contributions from the sky. Fig. 15 shows a true-color composite of an upward-looking fisheye view of the MODTRAN-created skydome radiance, generated using uniform sampling across the sky.

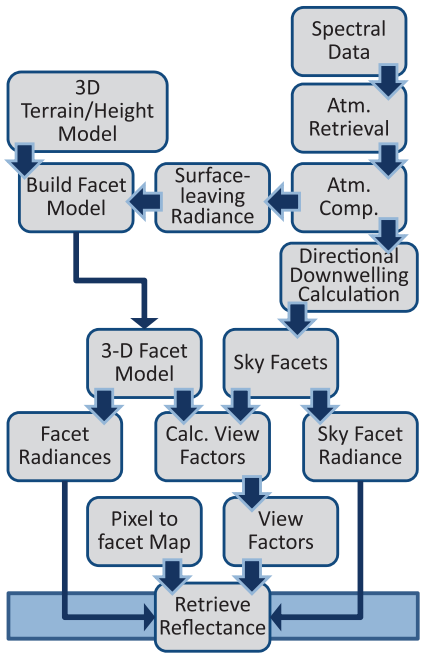


Fig. 14. The Radiosity reflectance retrieval workflow uses a series of operations to estimate reflectance using a 3-d spatial model and radiance data.

Fig. 15. True-color composite of an upward-looking fisheye view of the MODTRAN-created skydome radiance, generated using uniform sampling across the sky.

The directional sky data is interpolated to create a facetized skydome consisting of approximately 25,000 facets, which model changes in brightness across the skydome. The use of a facetized skydome with directional radiance contributions allows for more accurate illumination prediction in shadow, where the brightest portion of the sky (nearby the sun) is generally blocked by raised surface geometry in the scene and a Lambertian sky assumption would provide incorrect results. The facetized skydome is modeled at a sufficient distance such that, when traversing from one spatial location of a scene to another, the observer's perspective of the skydome does not change.

The next step in the processing chain is to facetize the scene into discrete patches that have uniform radiance and are on the same surface. An initial scene facetization is created using the set of *XYZ* coordinates from the LiDAR point cloud or other rasterized elevation data. This surface is registered with the radiance data, and then the facets are iteratively divided until each facet is radiometrically uniform across its surface. This division breaks the scene into facets that are sunlit or in shadow and minimizes any issues that are caused by nonuniform intensity across the surface as it interacts with other surfaces within the scene.

The pixel to facet map is generated by using the facetized elevation data and the registered ground-leaving radiance data. Then, radiosity values are assigned to each facet equal to the average surface-leaving radiance of pixels within that facet. Each facet is also tested to determine if it is shaded or in direct solar illumination. The sun is treated as a point source using the direct solar MODTRAN output term, retrieved during the initial atmospheric characterization step as the radiant intensity. The test examines whether the center $(x,y,z)$ location of each facet either points away from the sun, or is obscured by other objects in the scene that block the line of sight between the facet's center and the solar location. If either test is true, that facet is flagged as being in shadow.

For facets not seen by the sensor, such as the sides of a building, radiosity is estimated using either the average scene radiance or separate averages from the visible sun-lit and shaded facets. Even though a surface may be hidden from the sensor, it may have a significant impact on the illumination of objects observed within the scene, such as a potential target of interest in shadow adjacent to a large building. Therefore, an accurate representation of the unseen surface's radiosity is important to estimate.

The last unknown in the radiosity equation is the form factor between scene facets and other scene/sky facets, $F_{ji}$. An OpenGL implementation of the hemi-cube algorithm [97] has been integrated into the MATLAB code to efficiently calculate the form factors between each facet to all the other facets.

The sensor data can then be converted to reflectance by dividing the retrieved ground-leaving radiance at the pixel level by the illumination estimate of the pixel's assigned facet. The proposed method is validated using scenes generated from DIRSIG [98].

### *B. Results and Discussion*

The proposed technique is applied to the WorldView-2 image, as well as co-located LiDAR data on a 128 by 128 pixel subset that includes a large shadow area as shown in Fig. 16. The use of a subset of the full data reduced run-times and memory requirements.

The digital surface model (DSM) generated from the data orthorectified to a 0.5 m *x*-*y* grid is used to create the geometry model. Fig. 17 shows the DSM of the area processed.

MODTRAN and the WorldView-2 relative spectral response functions are used to calculate the transmission and path radiance for each band in order to convert the WorldView-2 data to surface-leaving radiance. Then, an in-scene correction is used to further refine the values. The in-scene techniques rely on the atmospheric effects' invariability between nearby pixels and the presence of two pixels of the same material in sunlight and shade. Within this step, the user manually selects two background pixels of the same apparent material, one in sun and the other in shadow. The path radiance and transmission estimates

Fig. 16. The image subset used for the calculations has a large shadow cast by the building in the middle of the image.

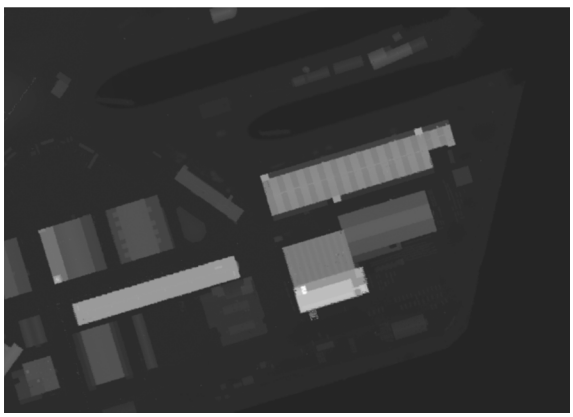

Fig. 17. A DSM model created from the LiDAR data provides the basis for the geometry model.

are modified until the radiosity retrieval for those two pixels results in the same reflectance being retrieved for both pixels. The fundamental basis of this approach is the fact that when the proper atmosphere and scene geometry is applied, the same reflectance should be obtained for a given material using the radiosity approach, regardless of whether it is sunlit or in shadow. Lambertian reflectance is assumed for all in-scene surfaces.

Once the data is converted to surface-leaving radiance, the radiosity technique is applied to the WorldView-2 subset selected for analysis. The facetization of the chip from the LiDAR data and surface-leaving radiance resulted in 3001 facets. Fig. 18 shows a wire-frame representation of the facets. A pixel to facet map is then created, which is used to assign radiosity values to the various scene surfaces, as well as determine the illumination on a per-pixel basis for the reflectance retrieval.

A reflectance retrieval using the radiosity equation is then performed. A true-color (RGB bands 5,3,2) composite of reflectance output obtained by the radiosity process (Fig. 19) shows the increased detail revealed in the shaded area. Relative spectral color and intensity of the road matches well between sunlit and shaded areas, but issues in reflectance retrieval persist at the shadow edges where pixels may be partially sunlit.

To further demonstrate the improvements, Figs. 20 and 21 show principal component (PC) transforms of the radiance data and the retrieved reflectance, respectively. The transform of the

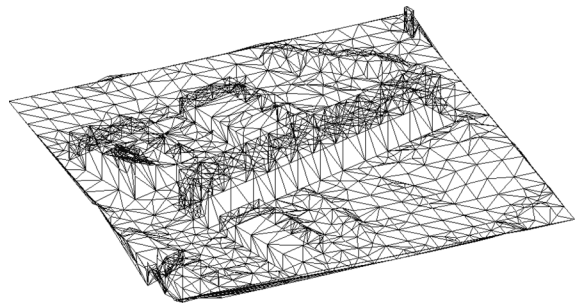

Fig. 18. The facetization process creates a new geometry model that accounts for surface orientation and the measured radiance differences.

Fig. 19. The image subset after applying the radiosity reflectance retrieval shows detail in the shaded region with structure similar to the adjacent sunlit region. Edge effects show up as dark pixels on the transitions between sunlit and shaded areas.

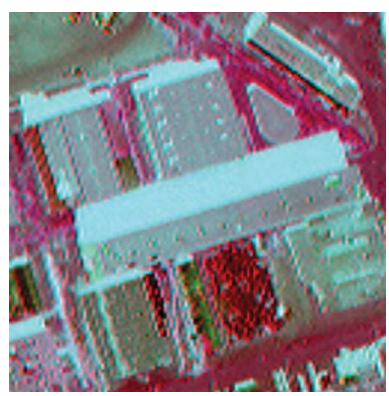

Fig. 20. A color composite from the first three principle components of the radiance transform shows the similar materials in the scene. The shaded region shows up as a different material than the surrounding surfaces.

radiance data shows little detail in the shaded region and appears as a different material class than the adjacent roads. After the radiosity reflectance retrieval, the PC transform shows the shaded region to more closely match the adjacent roads.

## V. Conclusion

This paper summarized the outcome of the 2012 IEEE GRSS Data Fusion Contest, including the contributions of the three winning teams:

1) In Section II, a new metric to assess urban density that takes into account all three spatial dimensions of an urban area was proposed. Due to the 3-dimensional nature of human

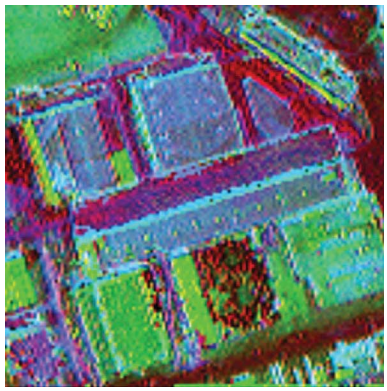

Fig. 21. A color composite from the first three principle components of the retrieved reflectance shows improved detail in the shaded region. The area now appears similar to the adjacent roads rather than a different material.

settlements, urban planning and decision making should be based on information sources that account for both the horizontal and vertical dimensions of a city to enable an integrated and more holistic assessment of the *builtscape* [21]. The derived UD map and statistics highlight the validity and suitability of the proposed metric as a useful measure to evaluate human settlement density and its distinct spatial patterns for different types of urban LU.

2) Section III illustrated a simulation based method for image interpretation and change detection, jointly using LiDAR and SAR data. To this end, the LiDAR data was decomposed into DSM, DEM, nDSM as well as individual building and wall models. Exploiting the simulated images of all these models, different layers (double reflections, layover, shadow, ground and background) are generated for the whole scene as well as for single buildings. Analyzing the TerraSAR-X image in the shadow and ground layer, positive changes were detected with respect to the LiDAR data. Analyzing building wall layover in TerraSAR-X images, signature patterns were identified, serving an object based description of façades. The results indicated that simulation techniques can support SAR image interpretation as well as change detection for local scenes and individual urban objects.
3) In Section IV, the radiosity technique was applied to retrieve reflectance for a subset of the WorldView-2 and LiDAR data. The results showed an improved capability to characterize shaded regions, demonstrating the utility of modeling illumination from nearby objects to improve the results for shaded regions.

As a final remark on the Contest, even though several different research topics were investigated by the various teams, none of the manuscripts exploited the three provided data sets in full synergy. In fact, the bulk of contributions either used multi-spectral and LiDAR or SAR and LiDAR data only. This may demonstrate the great difficulties encountered when fusing VHR multi-spectral and SAR data or fusing the three modalities together.

One possible explanation for this is that the information content in SAR data is typically characterized by three types of geometric effects, namely layover, shadow, and foreshortening [99]. These effects are more evident in VHR SAR imagery covering urban areas because human settlements are characterized by distinct and very individual 3-dimensional structures that comprise regularly and irregularly arranged LC objects of different shape, size and/or orientation [100]–[102]. Only when the viewing direction of the SAR and optical sensor is orthogonal [103], the fusion of these two data is possible and reasonable. However, this configuration is not the usual case. In contrast, the fusion of SAR and LiDAR does not suffer from such problems as the geometric projection is already considered in the SAR simulation procedure.

In the context of urban mapping with optical and LiDAR data, the additional information provided by VHR SAR systems (e.g., intensity, texture, coherence, etc.) can actually be of little help if geometric distortions predominate. This is because these effects hold the potential to hamper nearly every stage of the analysis task, including precise coregistration of the different data types, data fusion at different levels, and most importantly, feature extraction and classification.

It is also noteworthy that the fusion of all three data sources is application driven and may not be of interest for all possible studies. For instance, for the adjoint radiosity processing, SAR data was not considered as it does not add any useful information to improve surface reflectance retrieval.

## Acknowledgment

The authors and IEEE GRSS DFTC would like to express their great appreciation to DigitalGlobe, Astrium Services, and USGS for providing the data sets used in this study. The DFTC is also particularly thankful to Mr. Ed Locher from DigitalGlobe, Dr. Oliver Lang and Dr. Parivash Lumsdon from Astrium Services, and Dr. Karl Heidemann from USGS, for their continuous support throughout the 2012 Data Fusion Contest.

## References

[1] IEEE GRSS data fusion technical committee, 2012 [Online]. Available: http://www.grss-ieee.org/community/technical-committees/data-fusion/

[2] L. Alparone, L. Wald, J. Chanussot, C. Thomas, P. Gamba, and L. Bruce, "Comparison of pansharpening algorithms: Outcome of the 2006 GRS-S data-fusion contest," *IEEE Trans. Geosci. Remote Sens.*, vol. 45, no. 10, pp. 3012–3021, Oct. 2007.

[3] F. Pacifici, F. Del Frate, W. Emery, P. Gamba, and J. Chanussot, "Urban mapping using coarse SAR and optical data: Outcome of the 2007 GRSS data fusion contest," *IEEE Geosci. Remote Sens. Lett.*, vol. 5, no. 3, pp. 331–335, Jul. 2008.

[4] G. Licciardi, F. Pacifici, D. Tuia, S. Prasad, T. West, F. Giacco, C. Thiel, J. Inglada, E. Christophe, J. Chanussot, and P. Gamba, "Decision fusion for the classification of hyperspectral data: Outcome of the 2008 GRS-S data fusion contest," *IEEE Trans. Geosci. Remote Sens.*, vol. 47, no. 11, pp. 3857–3865, Nov. 2009.

[5] N. Longbotham, F. Pacifici, T. Glenn, A. Zare, M. Volpi, D. Tuia, E. Christophe, J. Michel, J. Inglada, J. Chanussot, and Q. Du, "Multi-modal change detection, application to the detection of flooded areas: Outcome of the 2009–2010 data fusion contest," *IEEE J. Sel. Topics Appl. Earth Observ. Remote Sens.*, vol. 5, no. 1, pp. 331–342, Feb. 2012.

[6] F. Pacifici and Q. Du, "Foreword to the special issue on optical multi-angular data exploitation and outcome of the 2011 GRSS data fusion contest," *IEEE J. Sel. Topics Appl. Earth Observ. Remote Sens.*, vol. 5, no. 1, pp. 3–7, Feb. 2012.

[7] J. Zhang, "Multi-source remote sensing fusion: status and trends," *Int. J. Image and Data Fusion*, vol. 1, no. 1, pp. 5–24, Mar. 2012.

[8] P. Hyde, R. Dubayah, W. Walker, J. B. Blair, M. Hofton, and C. Hunsaker, "Mapping forest structure for wildlife habitat analysis using multi-sensor (LiDAR, SAR/InSAR, ETM+, QuickBird) synergy," *Remote Sens. Environ.*, vol. 102, pp. 63–73, 2006.

[9] D. Goodenough, H. Chen, A. Dyk, G. Hobart, and A. Richardson, "Data fusion study between polarimetric SAR, hyperspectral and LiDAR data for forest information," in *Proc. IEEE Int. Geoscience and Remote Sensing Symp., IGARSS 2008*, Jul. 2008, vol. 2, pp. II-281–II-284.

[10] M. Benson, L. Pierce, K. Bergen, K. Sarabandi, K. Zhang, and C. Ryan, "Extrapolation of LiDAR for forest structure estimation using SAR, InSAR, and optical data," in *Proc. IEEE Int. Geoscience and Remote Sensing Symp., IGARSS 2010*, Jul. 2010, pp. 1633–1636.

[11] J. M. Kellndorfer, W. S. Walker, E. LaPoint, K. Kirsch, J. Bishop, and G. Fiske, "Statistical fusion of LiDAR, InSAR, and optical remote sensing data for forest stand height characterization: A regional-scale method based on LVIS, SRTM, Landsat ETM plus, and ancillary data sets," *J. Geophysical Research*, vol. 115, Jan. 2010.

[12] M. Benson, L. Pierce, K. Bergen, K. Sarabandi, K. Zhang, and C. Ryan, "Forest structure estimation using SAR, LiDAR, and optical data in the Canadian boreal forest," in *Proc. IEEE Int. Geoscience and Remote Sensing Symp., IGARSS 2011*, Jul. 2011, pp. 2609–2612.

[13] M. Lennon, N. Thomas, V. Mariette, S. Babichenko, and G. Mercier, "Oil slick detection and characterization by satellite and airborne sensors: Experimental results with SAR, hyperspectral and LiDAR data," in *Proc. IEEE Int. Geoscience and Remote Sensing Symp., IGARSS 2005*, Jul. 2005, vol. 1.

[14] M. Dalponte, L. Bruzzone, and D. Gianelle, "Fusion of hyperspectral and LiDAR remote sensing data for classification of complex forest areas," *IEEE Trans. Geosci. Remote Sens.*, vol. 46, no. 5, pp. 1416–1427, May 2008.

[15] T. Kurz, S. Buckley, J. Howell, and D. Schneider, "Close range hyperspectral and LiDAR data integration for geological outcrop analysis," in *1st Workshop Hyperspectral Image and Signal Processing: Evolution in Remote Sensing, WHISPERS'09*, Aug. 2009, pp. 1–4.

[16] K. Niemann, G. Frazer, R. Loos, and F. Visintini, "LiDAR-guided analysis of airborne hyperspectral data," in *1st Workshop Hyperspectral Image and Signal Processing: Evolution in Remote Sensing, WHISPERS'09*, Aug. 2009, pp. 1–4.

[17] M. Frank, Z. Pan, B. Raber, and C. Lenart, "Vegetation management of utility corridors using high-resolution hyperspectral imaging and LiDAR," in *2nd Workshop Hyperspectral Image and Signal Processing: Evolution in Remote Sensing (WHISPERS)*, Jun. 2010, pp. 1–4.

[18] A. Brook, E. Ben-Dor, and R. Richter, "Fusion of hyperspectral images and LiDAR data for civil engineering structure monitoring," in *2nd Workshop Hyperspectral Image and Signal Processing: Evolution in Remote Sensing (WHISPERS)*, Jun. 2010, pp. 1–5.

[19] C. Lenart, P. Burai, A. Smailbegovic, T. Biro, Z. Katona, and R. Andricevic, "Multi-sensor integration and mapping strategies for the detection and remediation of the red mud spill in Kolontar, Hungary: Estimating the thickness of the spill layer using hyperspectral imaging and LiDAR," in *3rd Workshop on Hyperspectral Image and Signal Processing: Evolution in Remote Sensing (WHISPERS)*, Jun. 2011, pp. 1–4.

[20] M. Shimoni, G. Tolt, C. Perneel, and J. Ahlberg, "Detection of vehicles in shadow areas using combined hyperspectral and LiDAR data," in *Proc. IEEE Int. Geoscience and Remote Sensing Symp., IGARSS 2011*, Jul. 2011, pp. 4427–4430.

[21] P. Gamba, F. Dell'Acqua, F. Cisotta, and G. Lisini, "High resolution InSAR "builtscape" improvement using LIDAR as ancillary data," in *Proc. IEEE Int. Geoscience and Remote Sensing Symp., IGARSS 2004*, Anchorage, AK, USA, Sep. 20–24, 2004, vol. 3, pp. 1808–1811.

[22] H. Taubenböck, M. Wegmann, A. Roth, H. Mehl, and S. Dech, "Urbanization in India—Spatiotemporal analysis using remote sensing data," *Computers, Environment and Urban Systems*, vol. 33, no. 3, pp. 179–188, May 2009.

[23] M. Pesaresi, M. Halkia, and G. Ouzounis, "Quantitative estimation of settlement density and limits based on textural measurements," in *Proc. Joint Urban Remote Sensing Event (JURSE)*, Apr. 2011, pp. 89–92.

[24] P. Tompalski and P. Wezyk, "LiDAR and VHRS data for assessing living quality in cities—An approach based on 3D indices," *ISPRS Int. Archives of the Photogrammetry, Remote Sensing and Spatial Information Sciences*, vol. XXXIX-B6, pp. 173–176, 2012.

[25] X.-Z. Pan, Q.-G. Zhao, J. Chen, Y. Liang, and B. Sun, "Analyzing the variation of building density using high spatial resolution satellite images: The example of Shanghai city," *Sensors*, vol. 8, no. 4, pp. 2541–2550, 2008.

[26] B. Yu, H. Liu, J. Wu, Y. Hu, and L. Zhang, "Automated derivation of urban building density information using airborne LiDAR data and object-based method," *Landscape and Urban Planning*, vol. 98, no. 3–4, pp. 210–219, Dec. 2010.

[27] T. Esch, V. Himmler, G. Schorcht, M. Thiel, T. Wehrmann, F. Bachofer, C. Conrad, M. Schmidt, and S. Dech, "Large-area assessment of impervious surface based on integrated analysis of single-date Landsat-7 images and geospatial vector data," *Remote Sens. Environ.*, vol. 113, no. 8, pp. 1678–1690, Aug. 2009.

[28] P. Leinenkugel, T. Esch, and M. Gähler, "Settlement detection and impervious surface estimation in the Mekong Delta using optical and SAR remote sensing data," *Remote Sens. Environ.*, vol. 115, no. 12, pp. 3007–3019, Dec. 2011.

[29] G. Xian and M. Crane, "An analysis of urban thermal characteristics and associated land cover in Tampa Bay and Las Vegas using Landsat satellite data," *Remote Sens. Environ.*, vol. 104, no. 2, pp. 147–156, Sept. 2006.

[30] F. Yuan and M. Bauer, "Comparison of impervious surface area and normalized difference vegetation index as indicators of surface urban heat island effects in Landsat imagery," *Remote Sens. Environ.*, vol. 106, no. 3, pp. 375–386, Feb. 2007.

[31] Q. Weng, "Remote sensing of impervious surfaces in the urban areas: Requirements, methods, and trends," *Remote Sens. Environ.*, vol. 117, pp. 34–49, Feb. 2012.

[32] D. Haase, "Effects of urbanisation on the water balance—A long-term trajectory," *Environmental Impact Assessment Review*, vol. 29, no. 4, pp. 211–219, Jul. 2009.

[33] K. Sawaya, L. Olmanson, N. Heinert, P. Brezonik, and M. Bauer, "Extending satellite remote sensing to local scales: Land and water resource monitoring using high-resolution imagery," *Remote Sens. Environ.*, vol. 88, no. 1–2, pp. 144–156, Nov. 2003.

[34] M. B. Pont and P. Haupt, , M. B. Pont and P. Haupt, Eds., *Spacematrix: Space, Density and Urban Form*. Rotterdam, The Netherlands: NAi Publishers, 2010.

[35] E. Salomons and M. B. Pont, "Urban traffic noise and the relation to urban density, form, and traffic elasticity," *Landscape and Urban Planning*, vol. 108, no. 1, pp. 2–16, Oct. 2012.

[36] R. Gluch and K. Ridd, , T. Rashed and C. Jürgens, Eds., "The V-I-S model: Quantifying the urban environment," in *Remote Sensing of Urban and Suburban Areas*. Dordrecht, The Netherlands: Springer, 2010, pp. 85–116.

[37] S. Faryadi and S. Taheri, "Interconnections of urban green spaces and environmental quality of Tehran," *Int. J. Environmental Research*, vol. 3, no. 2, pp. 199–208, 2009.

[38] M. Hur, J. Nasar, and B. Chun, "Neighborhood satisfaction, physical and perceived naturalness and openness," *J. Environ. Psychol.*, vol. 30, no. 1, pp. 52–59, Mar. 2010.

[39] E. Leslie, T. Sugiyama, D. Ierodiaconou, and P. Kremer, "Perceived and objectively measured greenness of neighborhoods: Are they measuring the same thing," *Landscape and Urban Planning*, vol. 95, no. 1–2, pp. 28–33, Mar. 2010.

[40] J. Tilt, T. Unfried, and B. Roca, "Using objective and subjective measures of neighborhood greenness and accessible destinations for understanding walking trips and BMI in Seattle, Washington," *Amer. J. Health Promotion*, vol. 21, no. 4, pp. 371–379, 2007.

[41] E. Schöpfer, S. Lang, and T. Blaschke, "A Green index incorporating remote sensing and citizen's perception of green space," in *Proc. ISPRS Joint Conf. 3rd Int. Symp. Remote Sensing and Data Fusion Over Urban Areas (URBAN 2005) and the 5th Int. Symp. Remote Sensing of Urban Areas (URS 2005)*, M. Moeller and E. Wentz, Eds., Tempe, AZ, USA, Mar. 14–16, 2005, vol. 37, pp. 1–6, Part 5/W1.

[42] B. Ong, "Green plot ratio: An ecological measure for architecture and urban planning," *Landscape and Urban Planning*, vol. 63, no. 4, pp. 197–211, May 2003.

[43] C. Pohl and J. van Genderen, "Multisensor image fusion in remote sensing: Concepts, methods and applications," *Int. J. Remote Sens.*, vol. 19, no. 5, pp. 823–854, May 1998.

[44] R. Richter, D. Schläpfer, and A. Müller, "An automatic atmospheric correction algorithm for visible/NIR imagery," *Int. J. Remote Sens.*, vol. 27, no. 10, pp. 2077–2085, May 2006.

[45] U. Gangkofner, P. Pradhan, and D. Holcomb, "Optimizing the highpass filter addition technique for image fusion," *Photogramm. Eng. Remote Sens.*, vol. 74, no. 9, pp. 1107–1118, Sept. 2008.

[46] C. Tucker, "Red and photographic infrared linear combinations for monitoring vegetation," *Remote Sens. Environ.*, vol. 8, no. 2, pp. 127–150, May 1979.

[47] L. Zevenbergen and C. Thorne, "Quantitative analysis of land surface topography," *Earth Surface Processes and Landforms*, vol. 12, no. 1, pp. 12–56, Jan./Feb. 1987.

[48] G. Priestnall, J. Jafaar, and A. Duncan, "Extracting urban features from LiDAR digital surface models," *Computers, Environment and Urban Systems*, vol. 24, no. 2, pp. 65–78, Mar. 2000.

[49] U. Benz, P. Hofmann, G. Willhauck, I. Lingenfelder, and M. Heynen, "Multi-resolution, object-oriented fuzzy analysis of remote sensing data for GIS-ready information," *ISPRS J. Photogramm. Remote Sens.*, vol. 58, no. 3–4, pp. 239–258, Jan. 2004.

[50] T. Blaschke, S. Lang, and G. Hay, , T. Blaschke, S. Lang, and G. Hay, Eds*., Object-Based Image Analysis for Remote Sensing. Spatial Concepts for Knowledge-Driven Remote Sensing Applications*. Berlin, Germany: Springer, 2008.

[51] T. Blaschke, "Object-based image analysis for remote sensing," *ISPRS J. Photogramm. Remote Sens.*, vol. 65, no. 1, pp. 2–16, Jan. 2010.

[52] G. Hay and G. Castilla, , T. Blaschke, S. Lang, and G. Hay, Eds., "Geographic object-based image analysis (GEOBIA): A new name for a new discipline," in *Object-Based Image Analysis. Spatial Concepts for Knowledge-Driven Remote Sensing Applications*. Berlin, Germany: Springer, 2008, pp. 75–89.

[53] W. Zhou and A. Troy, "An object-oriented approach for analyzing and characterizing urban landscape at the parcel level," *Int. J. Remote Sens.*, vol. 29, no. 11, pp. 3119–3135, Jun. 2008.

[54] W. Zhou, G. Huang, A. Troy, and M. Cadenasso, "Object-based land cover classification of shaded areas in high spatial resolution imagery of urban areas: A comparison study," *Remote Sens. Environ.*, vol. 113, no. 8, pp. 1769–1777, Aug. 2009.

[55] M. Kim, M. Madden, and B. Xu, "GEOBIA vegetation mapping in Great Smoky Mountains National Park with spectral and non-spectral ancillary information," *Photogramm. Eng. Remote Sens.*, vol. 76, no. 2, pp. 137–149, Feb. 2010.

[56] B. Salehi, Y. Zhang, M. Zhong, and V. Dey, "Object-based classification of urban areas using VHR imagery and height points ancillary data," *Remote Sens.*, vol. 4, no. 8, pp. 2256–2276, Aug. 2012.

[57] C. Berger, M. Voltersen, I. Walde, S. Hese, and C. Schmullius, "Robust extraction of urban land cover information from HSR multi-spectral and LiDAR data," *IEEE J. Sel. Topics Appl. Earth Observ. Remote Sens.*, accepted for publication.

[58] *eCognition Developer 8.7.1. Reference Book*. Munich, Germany: Trimble Documentation, 2012.

[59] C. Burnett and T. Blaschke, "A multi-scale segmentation/object relationship modelling methodology for landscape analysis," *Ecological Modelling*, vol. 168, no. 3, pp. 233–249, Oct. 2003.

[60] B. Koch, M. Jochum, E. Ivitis, and M. Dees, "Pixelbasierte klassifizierung im Vergleich und zur Ergänzung zum objektbasierten Verfahren," *Photogrammetrie, Fernerkundung, Geoinformation*, vol. 3, pp. 195–204, 2003.

[61] M. Baatz, C. Hoffmann, and G. Willhauck, , T. Blaschke, S. Lang, and G. Hay, Eds., "Progressing from object-based to object-oriented image analysis," in *Object-Based Image Analysis. Spatial Concepts for Knowledge-Driven Remote Sensing Applications*. Berlin, Germany: Springer, 2008, pp. 29–42.

[62] J. Johnson, "Building footprints as of June 2011," 2012 [Online]. Available: https://data.sfgov.org/Facilities-and-Structures/Building-Footprints-Zipped-Shapefile-Format-/jezr-5bxm

[63] S. Stehman and R. Czaplewski, "Design and analysis for thematic map accuracy assessment: Fundamental principles," *Remote Sens. Environ.*, vol. 64, no. 3, pp. 331–344, Jun. 1998.

[64] J. Cohen, "A coefficient of agreement for nominal scales," *Educational and Psychological Measurement*, vol. 20, no. 1, pp. 37–46, Apr. 1960.

[65] M. Bauer, B. Loeffelholz, and B. Wilson, , Q. Weng, Ed., "Estimating and mapping impervious surface area by regression analysis of Landsat imagery," in *Remote Sensing of Impervious Surfaces*. Boca Raton, FL, USA: CRC Press, 2008, pp. 3–19.

[66] A. Elmore and S. Guinn, "Synergistic use of Landsat multispectral scanner with GIRAS land-cover data to retrieve impervious surface area for the Potomac River Basin in 1975," *Remote Sens. Environ.*, vol. 114, no. 10, pp. 2384–2391, Oct. 2010.

[67] L. Luo and G. Mountrakis, "Integrating intermediate inputs from partially classified images within a hybrid classification framework: An impervious surface estimation example," *Remote Sens. Environ.*, vol. 114, no. 6, pp. 1220–1229, Jun. 2010.

[68] Q. Weng, , Q. Weng, Ed., "Remote sensing of impervious surfaces," in *Remote Sensing of Impervious Surfaces*. Boca Raton, FL, USA: CRC Press, 2008, pp. XV–XXVI.

[69] L. Yang, C. Huang, C. Homer, B. Wylie, and M. Coan, "An approach for mapping large-area impervious surfaces: Synergistic use of Landsat-7 ETM+ and high spatial resolution imagery," *Can. J. Remote Sens.*, vol. 29, no. 2, pp. 230–240, Apr. 2003.

[70] M. Wynne, "Zoning use districts," 2012 [Online]. Available: https://data.sfgov.org/Geography/Zoning-Districts/mici-sct2

[71] J. Eberle and C. Berger, "Urban density (UD) mapping results for the city of San Francisco," 2012 [Online]. Available: http://www.sf.maps.essi-blog.org

[72] G. Franceschetti, A. Iodice, D. Riccio, and G. Ruello, "SAR raw signal simulation for urban structures," *IEEE Trans. Geosci. Remote Sens.*, vol. 41, no. 9, pp. 1986–1995, Sep. 2003.

[73] S. Auer, S. Hinz, and R. Bamler, "Ray-tracing simulation techniques for understanding high-resolution SAR images," *IEEE Trans. Geosci. Remote Sens.*, vol. 48, no. 3, pp. 1445–1456, Mar. 2010.

[74] T. Balz and U. Stilla, "Hybrid GPU-based single-and double-bounce SAR simulation," *IEEE Trans. Geosci. Remote Sens.*, vol. 47, no. 10, pp. 3519–3529, Oct. 2009.

[75] D. Brunner, G. Lemoine, H. Greidanus, and L. Bruzzone, "Radar imaging simulation for urban structures," *IEEE Geosci. Remote Sens. Lett.*, vol. 8, no. 1, pp. 68–72, Jan. 2011.

[76] H. Hammer and K. Schulz, "SAR-simulation of large urban scenes using an extended ray tracing approach," in *2011 Joint Urban Remote Sensing Event (JURSE)*, Apr. 2011, pp. 289–292.

[77] R. Guida, A. Iodice, D. Riccio, and U. Stilla, "Model-based interpretation of high-resolution SAR images of buildings," *IEEE J. Sel. Topics Appl. Earth Observ. Remote Sens.*, vol. 1, no. 2, pp. 107–119, Jun. 2008.

[78] T. Balz, , U. Soergel, Ed., "SAR simulation of urban areas: Techniques and applications," in *Radar Remote Sensing of Urban Areas*, ser. Remote Sensing and Digital Image Processing. Heidelberg, Germany: Springer, 2010, pp. 215–231.

[79] D. Brunner, G. Lemoine, and L. Bruzzone, "Earthquake damage assessment of buildings using VHR optical and SAR imagery," *IEEE Trans. Geosci. Remote Sens.*, vol. 48, no. 5, pp. 2403–2420, May 2010.

[80] F. Bovolo and L. Bruzzone, "A detail-preserving scale-driven approach to change detection in multitemporal SAR images," *IEEE Trans. Geosci. Remote Sens.*, vol. 43, no. 12, pp. 2963–2972, Dec. 2005.

[81] F. Bovolo and L. Bruzzone, "A split-based approach to unsupervised change detection in large-size multitemporal images: Application to tsunami-damage assessment," *IEEE Trans. Geosci. Remote Sens.*, vol. 45, no. 6, pp. 1658–1670, Jun. 2007.

[82] A. Schmitt, B. Wessel, and A. Roth, "Curvelet approach for SAR image denoising, structure enhancement, and change detection," in *Proc. CMRT09*, Sep. 2009, vol. 38, pp. 151–156.

[83] F. Bovolo, C. Martin, and L. Bruzzone, "A novel hierarchical approach to change detection with very high resolution SAR images for surveillance applications," in *Proc. IEEE Int. Geoscience and Remote Sensing Symp., IGARSS 2012*, Jul. 2012.

[84] H. Arefi, P. d'Angelo, H. Mayer, and P. Reinartz, "Iterative approach for efficient digital terrain model production from CARTOSAT-1 stereo images," *J. Appl. Remote Sens.*, vol. 5, no. 1, Jun. 2001.

[85] S. Auer, "3D Synthetic Aperture Radar Simulation for Interpreting Complex Urban Reflection Scenarios," Ph.D. dissertation, Technische Universität München, Munich, Germany, 2011.

[86] J. Tao, G. Palubinskas, P. Reinartz, and S. Auer, "Interpretation of SAR images in urban areas using simulated optical and radar images," in *2011 Joint Urban Remote Sensing Event (JURSE)*, Apr. 2011, pp. 41–44.

[87] J. Tao, S. Auer, and P. Reinartz, "Detecting changes between a DSM and a high resolution SAR image with the support of simulation based separation of urban scenes," in *Proc. 9th Eur. Conf. Synthetic Aperture Radar, EUSAR 2012*, Apr. 2012, pp. 95–98.

[88] S. Auer, C. Gisinger, and R. Bamler, "Characterization of SAR image patterns pertinent to individual façades," in *Proc. IEEE Int. Geoscience and Remote Sensing Symp., IGARSS 2012*, Jul. 2012.

[89] D. Manolakis, D. Marden, and G. Shaw, "Hyperspectral image processing for automatic target detection applications," *Lincoln Lab. J.*, vol. 14, no. 1, pp. 79–114, 2003.

[90] C. Borel, K. Ewald, M. Manzardo, C. Wamsley, and J. Jacobson, "Adjoint radiosity based algorithms for retrieving target reflectances in urban area shadows," in *Proc. 6th EARSeL Imaging Spectroscopy SIG Workshop*, Mar. 2009, pp. 16–19.

[91] M. F. Cohen and J. R. Wallace, *Radiosity and Realisitc Image Synthesis*. New York: Academic Press Professional, 2003.

[92] F. X. Sillion and C. Puech, *Radiosity and Global Illumination*. San Diego, CA: Morgan Kaufmann, 1994.

[93] C. M. Goral, K. E. Torrance, D. P. Greenberg, Greenberg, and B. Battaile, "Modeling the interaction of light between diffuse surfaces," *Computer Graphics*, vol. 18, no. 3, pp. 215–224, 1999.

[94] Y. Yu, P. Debevec, J. Malik, and T. Hawkins, "Inverse global illumination: Recovering reflectance models of real scenes from photographs," in *Proc. 26th Annu. Conf. Computer Graphics and Interactive Techniques, SIGGRAPH'99*, 1999, pp. 215–224, ACM Press/Addison-Wesley Publishing Co..

[95] S. N. Pattanaik and S. P. Mudur, "The potential equation and importance in illumination computations," *Computer Graphics*, vol. 12, pp. 131–136, 1993.

[96] A. Berk, L. W. Bernstein, and D. C. Robertson, "Modtran: A Moderate Resolution Model for Lowtran7," Air Force Geophysical Laboratory, Hanscom Air Force Base, MA, Tech. Rep. aFGL-TR-83-0187, 1983.

[97] M. Cohen and D. Greenberg, "The hemi-cube: A radiosity solution for complex environments," *Computer Graphics*, vol. 19, no. 3, pp. 31–40, 1985.

[98] J. R. Schott, S. D. Brown, R. V. Raqueno, H. N. Gross, and G. Robinson, "An advanced synthetic image generation model and its application to multi/hyperspectral algorithm development," *Can. J. Remote Sens.*, vol. 25, no. 2, pp. 99–111, 1999.

[99] R. Raney, , F. Henderson and A. Lewis, Eds., "Radar fundamentals: Technical perspective," in *Principles and Applications of Imaging Radar. Manual of Remote Sensing*, 3rd ed. New York, NY, USA: Wiley, 1998, vol. 2, pp. 9–130.

[100] Y. Dong, B. Forster, and C. Ticehurst, "Radar backscatter analysis for urban environments," *Int. J. Remote Sens.*, vol. 18, no. 6, pp. 1351–1364, 1997.

[101] A. Brenner and L. Roessing, "Radar imaging of urban areas by means of very high-resolution SAR and interferometric SAR," *IEEE Trans. Geosci. Remote Sens.*, vol. 46, no. 10, pp. 2971–2982, Oct. 2008.

[102] *Radar Remote Sensing of Urban Areas*, U. Soergel, Ed. Heidelberg, Germany: Springer, 2010, pp. 277–1.

[103] G. Palubinskas, P. Reinartz, and R. Bamler, "Image acquisition geometry analysis for the fusion of optical and radar remote sensing data," *Int. J. Image and Data Fusion*, vol. 1, no. 3, pp. 271–282, 2010.


**Christian Berger** received the B.Sc. degree in geography and the M.Sc. degree in geoinformatics and remote sensing from the Friedrich-Schiller-University, Jena, Germany, in 2007 and 2010, respectively. In 2009, he joined the Department for Earth Observation, Friedrich-Schiller-University, Jena, Germany, where he is currently working towards the Ph.D. degree. His research focuses on the analysis of high spatial resolution multi-sensor Earth observation data to derive and evaluate land surface parameters for urban planning applications. Mr. Berger serves as a referee for the IEEE JOURNAL OF SELECTED TOPICS IN APPLIED EARTH OBSERVATIONS AND REMOTE SENSING, the *International Journal of Remote Sensing*, and *Information Fusion*.

**Michael Voltersen** received the B.Sc. degree in geography and the M.Sc. degree in geoinformatics and remote sensing from the Friedrich-Schiller-University, Jena, Germany, in 2008 and 2011, respectively. In 2010, he was a student apprentice at the Definiens Earth Sciences division (now Trimble GeoSpatial), Munich, Germany. In 2011, he joined the Department for Earth Observation, Friedrich-Schiller-University, Jena, Germany, where he was working on change analyses of thermokarst lakes as part of the ESA DUE Permafrost. As part of his Ph.D. studies, his current research focuses on the processing of high spatial resolution optical Earth observation data to extract and analyze land cover parameters and land use structures of urban areas.

**Robert Eckardt** received the B.Sc. degree in geography and the M.Sc. degree in geoinformatics and remote sensing from the Friedrich-Schiller-University, Jena, Germany, in 2008 and 2011, respectively.

In 2008 he joined the Department for Earth Observation, Friedrich-Schiller-University, Jena, Germany, where he is currently working as a research associate. His work focuses on an education initiative for applied synthetic aperture remote sensing (SAR-EDU). In 2012 Mr. Eckardt received the 2nd prize of the Young Scientist Award of the German, Austrian and Swiss Remote Sensing Societies (DGPF, OVG and SGPF)

**Jonas Eberle** received the B.Sc. degree in applied informatics from the University of Applied Sciences Ostwestfalen, Hoexter, Germany, and the M.Sc. degree in geoinformatics and remote sensing from the Friedrich-Schiller-University, Jena, Germany, in 2007 and 2011, respectively. Currently, he works at the Department for Earth Observation, Friedrich-Schiller-University Jena, Germany, as a research assistant and Ph.D. candidate. Within his research project, the Siberian Earth System Science Cluster (SIB-ESS-C), he focuses on automatic monitoring of time-series data and the development of web-based geographic information systems with open source software.

**Thomas Heyer** received the B.Sc. degree in geography from the Friedrich-Schiller-University, Jena, Germany, in 2010. He is currently pursuing the M.Sc. degree in geoinformatics and remote sensing at the same university. His present research focuses on concepts for rapid mapping of tsunami flooded coastal areas using remote sensing data and GIS modeling techniques.

**Nesrin Salepci** received the B.Sc. degree in geological engineering from Middle East Technical University, Ankara, Turkey, and the M.Sc. degree in geodesy and geoinformation science from the Berlin Institute of Technology, Berlin, Germany, in 2005 and 2010, respectively. She is currently working towards the Ph.D. degree within the Radar science group at the Department for Earth Observation, Friedrich-Schiller-University, Jena, Germany. Her main research focus is surface displacement monitoring by permanent scatterer interferometry.

**Sören Hese** received the M.Sc. degree in remote sensing, image processing, and applications from Dundee University, Dundee, UK, and the Ph.D. degree from the Technical University, Berlin, in 2001. He joined the German Aerospace Center (DLR) in 1997, and, since 2002, he is with the Department for Earth Observation, Friedrich-Schiller-University, Jena, Germany. Currently, he is an Assistant Professor at this department. His research interests include image object formation with high resolution Earth observation data, graph theoretical data analysis, landscape metrics in image data classification, and structural image data analysis for urban areas, flood and devastation mapping, and climate change related land cover change. He conducts and supervises research within the framework of national and international projects.

**Christiane Schmullius** received the M.A. degree in geography and remote sensing from the University of California, Santa Barbara, CA, USA, in 1986, and the Ph.D. degree from the Institute of Space Sciences, Free University, Berlin, Germany, in 1991. Her doctoral work focused on radar remote sensing of agricultural crops. From 1991 to 2000, she was a group leader of "Geomatics" with the German Aerospace Center (DLR). In 1994, she coordinated the SIR-C/X-SAR Science Team, and in 2000, she became DLR's project scientist for the Shuttle Radar Topography Mission (SRTM). She has coordinated several European Union (EU) projects in Siberia, especially on radar interferometry applications for climate change parameter mapping. Since 2000, she has been a professor of remote sensing with the Friedrich-Schiller-University, Jena, Germany.

**Junyi Tao** (S'12) was born in Wuhan, P.R. China in 1983. He received the Dipl.-Ing.(Univ.) degree in geodesy and geoinformatics from the Universität Stuttgart, Germany, in 2009.

Since October 2009, he has been a scientific collaborator with the Remote Sensing Technology Institute (IMF), German Aerospace Center (DLR), Oberpfaffenhofen, Germany, working in close cooperation with the chair of Remote Sensing Technology (LMF), Technische Universität München (TUM), Munich, Germany. In June 2012, he was a guest scientist at the Remote Sensing Laboratory, Department of Information Engineering and Computer Science, University of Trento, Trento, Italy. His research interests include SAR simulation, SAR image interpretation, multi-modal data fusion, and change detection. In particular, he focuses on the combination of LiDAR and SAR data with simulation techniques for object identification and change detection in urban areas.

**Stefan Auer** was born in Bad Reichenhall (Germany) in 1980. He received the Dipl.-Ing.(Univ.) degree in geodesy in December 2005 and the Dr.-Ing. degree in April 2011, both from the Technische Universität München (TUM).

Between February 2006 and December 2006 he was employed as scientific collaborator (half-time) at Remote Sensing Technology of TUM with focus on the extraction of building models from aerial laser scan data. Besides his scientific activities, he worked as a project engineer at Ingenieurbüro Wenger-Oehn, Salzburg, Austria. Since December 2006, he has been a full-time scientific collaborator at Remote Sensing Technology (TUM) and is concerned with the simulation and analysis of radar signal reflections in local urban scenes. In the course of his doctoral thesis, Stefan Auer spent three months as guest researcher at the Department of Electronic and Telecommunication Engineering (DIET) at the University of Naples "Federico II". His main interest is in supporting the interpretation of high resolution SAR images and interferometric SAR results by simulation methods. Moreover, he aims at investigating the nature of prominent SAR image signatures representing building structures. Based on this knowledge, he works on algorithms for characterizing signature patterns related to building facades.

**Richard Bamler** (M'95–SM'00–F'05) received his Diploma degree in electrical engineering, his Doctorate in Engineering, and his "Habilitation" in the field of signal and systems theory in 1980, 1986, and 1988, respectively, from the Technische Universität München, Germany. He worked at the university from 1981 to 1989 on optical signal processing, holography, wave propagation, and tomography.

He joined the German Aerospace Center (DLR), Oberpfaffenhofen, in 1989, where he is currently the Director of the Remote Sensing Technology Institute. In early 1994, Richard Bamler was a visiting scientist at Jet Propulsion Laboratory (JPL) in preparation of the SIC-C/X-SAR missions, and in 1996 he was guest professor at the University of Innsbruck. Since 2003 he has held a full professorship in remote sensing technology at the Technische Universität München as a double appointment with his DLR position. His teaching activities include university lectures and courses on signal processing, estimation theory, and SAR. Since 2010 he has been a member of the executive board of Munich Aerospace, a newly founded research and education project between Munich universities and extramural research institutions, incl. DLR. His research interests are in algorithms for optimum information extraction from remote sensing data with emphasis on SAR. This involves new estimation algorithms, like sparse reconstruction and compressive sensing. He has devised several high-precision algorithms for mono-static and bi-static SAR processing, SAR calibration and product validation, GMTI for traffic monitoring, SAR interferometry, phase unwrapping, persistent scatterer interferometry, and differential SAR tomography.

**Ken Ewald** received a B.S. degree in imaging science from Rochester Institute of Technology, and the M.S. degree in applied mathematics from Wright State University.

He is a senior scientist at Ball Aerospace and Technologies Corporation. He mainly works on algorithm development for processing of remotely sensed data, focusing on multi-and hyperspectral imagery in both the visible through shortwave infrared as well as the thermal infrared. A recent concentration of his work has been on automation and implementation of real-time data processing, occurring on-board the collection platform. He has also worked with various modeling and simulation capabilities, as well as testing and validation of data fusion techniques.

**Michael Gartley** received the B.S. degree in physics from Binghamton University, the M.S. degree in materials science from Rochester Institute of Technology (RIT), and the Ph.D. degree in imaging science from RIT.

He is an Associate Scientist in the Digital Imaging and Remote Sensing laboratory at the Rochester Institute of Technology (RIT). His current research interests focus on modeling and simulation of target phenomenology across modalities, with an emphasis on bi-directional reflectance distribution function and polarization effects. Prior to joining RIT, he was employed by ITT Space Systems where he was in involved in modeling and performance analysis of air and space-borne remote sensing platforms.

**John Jacobson** began his career as a 2nd Lieutenant at the Wright-Patterson Air Force Base in 1984, focusing on the fields of strategic missile systems performance analysis and radar signal analysis. After completing a Master's Degree in nuclear physics at the Air Force Institute of Technology, he developed code for performing atmospheric radiation transfer calculations, radiation fallout calculations, and radiation dose calculations for nuclear weapons detonations modeling. He subsequently spent nine years with the Nuclear Regulatory Commission (NRC) where he served as a certified health physicist and nuclear criticality safety engineer. He became an NRC Resident Inspector and participated in the development and implementation of the first nuclear oversight program for the Department of Energy (DOE) facilities, focusing on radiation and nuclear criticality safety at DOE production sites. In 2000, Mr. Jacobson returned to Wright-Patterson where his primary focus has been the development of multispectral and hyperspectral data analysis capabilities.

**Alan Buswell** received the Master of Science degree in electro-optics from the University of Dayton in 1986.

He is currently a Senior Remote Sensing Scientist with Ball Aerospace and Technologies Corporation in Fairborn, OH, where he has supported spectral remote sensing technology development for the last 15 years. His research interests include hyperspectral and multispectral algorithm development, processing system and operational implementation of spectral remote sensing systems, and data quality assessment.

**Qian Du** (S'98–M'00–SM'05) received her Ph.D. degree in electrical engineering from University of Maryland Baltimore County in 2000.

She was with the Department of Electrical Engineering and Computer Science, Texas A&M University-Kingsville, from 2000–2004. She joined the Department of Electrical and Computer Engineering at Mississippi State University in Fall 2004, where she is currently an Associate Professor. Her research interests include hyperspectral remote sensing image analysis, pattern classification, data compression, and neural networks.

Dr. Du currently serves as Co-Chair for the Data Fusion Technical Committee of IEEE Geoscience and Remote Sensing Society. She also serves as Associate Editor for IEEE JOURNAL OF SELECTED TOPICS IN APPLIED EARTH OBSERVATIONS AND REMOTE SENSING and Associate Editor for IEEE *Signal Processing Letters*. She received the 2010 Best Reviewer award from IEEE Geoscience and Remote Sensing Society. She is the General Chair for the 4th IEEE GRSS Workshop on Hyperspectral Image and Signal Processing: Evolution in Remote Sensing (WHISPERS) in Shanghai, China in 2012. Dr. Du is a member of SPIE, ASPRS, and ASEE.

**Fabio Pacifici** (S'03–M'10) received the Ph.D. degree in geoinformation from Tor Vergata University, Rome, Italy, in 2010. He also received the Laurea Specialistica (M.S.; *cum laude*) and Laurea (B.S.; *cum laude*) degrees in telecommunication engineering from the same University, in 2006 and 2003, respectively.

Since 2009, he is working at DigitalGlobe as R&D Scientist. Between 2005 and 2009, he collaborated as Visitor Scientist with the Department of Aerospace Engineering Sciences, University of Colorado, Boulder. He has been involved in various remote sensing projects supported by the European Space Agency.

His research activities include processing of remote sensing images, data fusion, feature extraction, active learning, and analysis of multi-angular and multi-temporal data. In particular, his research interests are related to the development of classification and change detection techniques for urban remote sensing applications using very high spatial resolution optical and/or synthetic aperture radar imagery, with special emphasis on machine learning. He is author (or co-author) of 15 scientific publications in referred international journals, two book chapters, and more than 50 contributions in international conferences.

Dr. Pacifici is the current Chair of the IEEE Geoscience and Remote Sensing Data Fusion Technical Committee and serves as Associate Editor for the IEEE JOURNAL OF SELECTED TOPICS IN APPLIED EARTH OBSERVATIONS AND REMOTE SENSING (JSTARS). He received the 2011 Best Reviewer Award from IEEE Geoscience and Remote Sensing Society for his service to IEEE JSTARS. He was the recipient of the 2009 Joint Urban Remote Sensing Event student paper competition. He received the first prize in the 2007, 2008 and 2009–2010 IEEE Geoscience and Remote Sensing Data Fusion Contest. He serves as a member of Technical Committee for the Joint Urban Event (since 2011), and for the International Geoscience and Remote Sensing Symposium (since 2009). He has been the Guest Editor of a special issue of JSTARS on multiangular remote sensing.